

Four-state discrimination for a pair of spin qubits via gate reflectometry

Aritra Sen¹ and András Pályi^{1,2}

¹*Department of Theoretical Physics, Institute of Physics,
Budapest University of Technology and Economics, Műegyetem rkp. 3., H-1111 Budapest, Hungary*

²*HUN-REN-BME-BCE Quantum Technology Research Group,
Budapest University of Technology and Economics, Műegyetem rkp. 3., H-1111 Budapest, Hungary*

(Dated: March 10, 2026)

Single-electron spin qubits defined in quantum dots are used as building blocks of a semiconductor-based quantum computer. Readout in a scaled-up version of such a quantum computer is expected to rely on the Pauli Spin Blockade (PSB) mechanism. A desired functionality of PSB readout is that it reveals two bits of information on the two spin qubits that are involved in the process, such that the four computational basis states can be discriminated. In this work, we propose and quantitatively analyze an experimental procedure, based on gate reflectometry, which enables this four-state discrimination in a single measurement. We provide an intuitive recipe to maximize the contrast between the quantum capacitances of the four basis states. Focusing on silicon double quantum dots equipped with a micromagnet, we quantify how amplifier noise and phonon-mediated relaxation influence readout fidelity. Our results highlight a realistic opportunity to mitigate the overhead of readout ancilla qubits in a spin-based quantum computer.

CONTENTS

References

14

I. Introduction	1
II. Double quantum dot Hamiltonian with two electrons	2
III. Four-state discrimination with quantum capacitance measurement	3
A. Capacitance contrast as a proxy for the quality of four-state discrimination	3
B. Assignment fidelity of four-state discrimination in the presence of amplifier noise	4
C. Maximizing the capacitance contrast	5
IV. Optimizing four-state discrimination in the presence of relaxation	7
V. Discussion	9
VI. Conclusions	9
Acknowledgments	9
A. Computing quantum capacitance of numerically obtained energy eigenstates without numerical differentiation	10
B. A more accurate perturbative description of the quantum capacitances at the singlet-triplet anticrossings	10
C. Phonon-induced relaxation rates in a silicon double quantum dot	10
1. Relaxation of a charge qubit	11
2. Relaxation between two-electron energy eigenstates	13

I. INTRODUCTION

Semiconductor quantum dot spin qubits have emerged as an important platform for quantum information processing, owing to their long coherence times, compatibility with industrial fabrication, and potential for dense integration [1–6]. The early proposal [1] identified the spin degree of freedom of a confined electron as a natural two-level system for quantum computation, and subsequent experiments demonstrated readout [7] and coherent control [8, 9] of single spins in gate-defined quantum dots. Over the past decade, rapid progress has been achieved in high-fidelity single- [10, 11] and two-qubit gates [12–14], the implementation of small multi-qubit processors [15–18], and elementary quantum simulation [19–21] and error-correction primitives [22–24]. In particular, silicon-based devices benefit from the availability of isotopically enriched material, which strongly suppresses hyperfine-induced decoherence [10, 25–32], and from their compatibility with established semiconductor technology [14, 33–41]. Complemented with an increasing activity in architecture design [42–46], these advances position semiconductor spin qubits as a promising route toward large-scale quantum computing and quantum simulation architectures.

A central ingredient of any scalable architecture is high-fidelity qubit readout. In a double quantum dot (DQD) with two spin qubits, readout is commonly realized via the Pauli spin blockade (PSB) mechanism [9, 47], which maps spin information onto charge configurations [8] upon tuning the DQD from the (1,1) to the (0,2) charge configuration. In its conventional implementation, the spin-dependent tunneling between the (1,1) and (0,2) charge states results in a blockade for triplet configurations, while singlet states hybridize with (0,2) and

can tunnel. This spin-to-charge conversion is typically detected by a proximal charge sensor, such as a quantum point contact [7, 8, 48, 49], a single-electron transistor [50–54], or a single-electron box [55, 56].

Alternatively, the spin information can also be converted into quantum capacitance by tuning the DQD from (1,1) into the vicinity of the (1,1)-(0,2) charge transition point; then, the quantum capacitance of the state is probed by dispersive gate-based reflectometry [39, 40, 57–65]. Towards scaling, gate reflectometry has the advantage that it avoids the footprint and wiring overhead of a nearby charge sensor. Here, we use the term ‘PSB readout’ in a broad sense, including charge sensing or capacitance measurement, as well as cases where spin-orbit interaction [64, 66–71], hyperfine interaction [8, 9, 72], or inhomogeneous magnetic fields [73, 74] break the spin selection rules.

PSB readout has three major modalities: (i) ancilla mode, where one of the two spins has a known state, and is used as a reference or ancilla for reading out the other spin; (ii) singlet-triplet mode, where the (1,1) singlet state is discriminated from the (1,1) triplet states; and (iii) parity mode, where the parallel-spin states (i.e., the polarized triplets) are distinguished from the antiparallel-spin states (i.e., the singlet and the unpolarized triplet).

In these modalities, PSB readout results in a single bit of information about the two spins. Is it possible to improve on this, i.e., to gain two bits, and hence discriminate all four spin states? A recent experiment [53] has demonstrated this functionality in a GaAs device by performing a sequence of three manipulation and readout steps, using optimized readout positions in the detuning-tunneling parameter space, careful control pulses to navigate between those positions, and charge sensing with a single electron transistor. Another experimental work [56] achieved three-state discrimination in a Si device, using a single electron box charge sensor, and implementing state discrimination using a hidden Markov model.

In this work, we propose, model, and quantitatively analyze a method to discriminate the four spin states in PSB readout, by measuring the quantum capacitance of the DQD with gate reflectometry in a single shot. This functionality is similar to simultaneous single-shot readout of two superconducting qubits. Simultaneous readout of two qubits have also been demonstrated. The method we describe here relies on the presence of level anticrossings and spin and charge hybridization in the detuning- and tunneling-dependent energy spectrum of the two-electron spin states, which in turn are caused by interdot tunneling and spin-mixing effects such as spin-orbit interaction or an inhomogeneous magnetic field. We focus on a Si-based two-electron DQD in the presence of a micromagnet, the latter enabling electrically driven spin control [73], and also opening the opportunity to four-state discrimination (4SD). We describe a way to maximize the contrast between the quantum capacitances of the four spin states. We also evaluate the contributions of phonon-mediated relaxation and amplifier noise to the

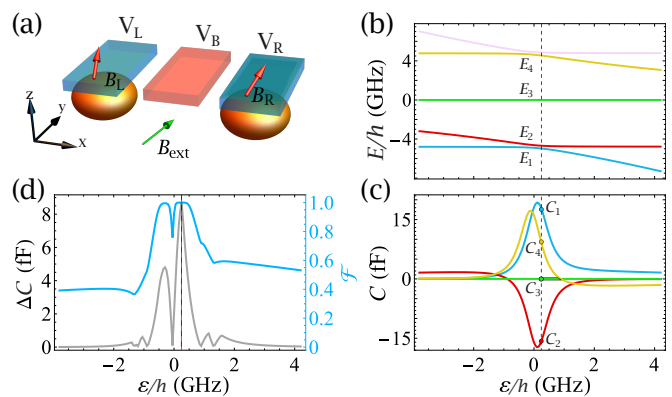


FIG. 1. **Four-state discrimination with a single quantum capacitance measurement.** (a) Schematics of the double quantum dot (DQD) in the presence of an inhomogeneous magnetic field. Energy spectrum (b) of the DQD, and quantum capacitances (c) of the energy eigenstates, as functions of detuning, for $t_0/h = 3.35$ GHz. Internal magnetic fields \mathbf{B}_L , \mathbf{B}_R in the two dots are different, and emerge as combinations of the homogeneous external magnetic field B_{ext} and the inhomogeneous micromagnet field. Magnetic-field parameters, related to \mathbf{B}_L and \mathbf{B}_R via Eqs. (2), (3), (4): $B_s = 171.8$ mT, $B_{a\parallel} = -2.5$ mT, and $B_{a\perp} = 9.8$ mT. (d) Quantum capacitance contrast ΔC (gray), and four-state assignment fidelity \mathcal{F} (blue), the latter computed with amplifier noise strength of $\sigma_C = 1$ fF. Gray dashed line in panels b, c, d indicate the maximum point of the capacitance contrast $\Delta C(\varepsilon)$.

readout error, and illustrate how the readout position can be optimized in the presence of those imperfections.

The rest of this paper is structured as follows. In Sec. II we specify our model Hamiltonian for the two-electron DQD in presence of inhomogeneous magnetic field. In Sec. III we describe the idea of four-state discrimination of a pair spin qubits using quantum capacitance measurement, and describe the figures of merits in terms of the capacitance contrast and the readout error. In Sec. IV we describe relaxation effects and how it influences readout error and the optimal readout position. Finally, we provide a discussion and outlook in Sec. V, and conclude in Sec. VI. The Appendix contains details of our calculations.

II. DOUBLE QUANTUM DOT HAMILTONIAN WITH TWO ELECTRONS

We focus on 4SD by a quantum capacitance measurement, in a two-electron DQD equipped with a micromagnet. The DQD with the micromagnet field is depicted in Fig. 1(a). The micromagnet enables electrically driven spin resonance via ac electric gate-voltage pulses. As we argue here, the presence of the micromagnet also opens an opportunity for 4SD.

The Hamiltonian of the DQD reads as follows:

$$H = H_{\text{Coulomb}} + H_{\text{on-site}} + H_{\text{tunneling}} + H_{\text{Zeeman}}, \quad (1a)$$

$$H_{\text{Coulomb}} = U(n_{L\uparrow}n_{L\downarrow} + n_{R\uparrow}n_{R\downarrow}), \quad (1b)$$

$$H_{\text{on-site}} = \sum_{j=L,R} \varepsilon_j n_j, \quad (1c)$$

$$H_{\text{tunneling}} = t_0 \sum_{s=\uparrow,\downarrow} c_{L,s}^\dagger c_{R,s} + h.c., \quad (1d)$$

$$H_{\text{Zeeman}} = \frac{1}{2} g\mu_B (\mathbf{B}_L \cdot \boldsymbol{\sigma}_L + \mathbf{B}_R \cdot \boldsymbol{\sigma}_R), \quad (1e)$$

Here, $j \in \{L,R\}$ is the dot label, $s \in \{\uparrow,\downarrow\}$ labels the two spin basis states, $c_{j,s}$ is the electron annihilation operator of dot j and spin s , $n_{j,s} = c_{j,s}^\dagger c_{j,s}$ is the number of electrons on dot j with spin s , and $n_j = \sum_s n_{j,s}$. The on-site Coulomb repulsion energy is denoted by U . The on-site energies of the dots are denoted by ε_j , and we define $\tilde{\varepsilon} = \varepsilon_L - \varepsilon_R$ and $\bar{\varepsilon} = (\varepsilon_L + \varepsilon_R)/2$. Later, we will use the *detuning* defined as $\varepsilon = \tilde{\varepsilon} - U$, i.e., ε is the detuning from the (1,1)-(0,2) charge transition point. To make our plots, we will set $\bar{\varepsilon} = 0$. The spin operators $\boldsymbol{\sigma}_j$ are Pauli spin operators of the two dots; e.g., $\sigma_{L,z} = n_{L,\uparrow} - n_{L,\downarrow}$.

For simplicity, we assume a trivial structure for the gate-voltage lever arms. In particular, we consider the quantum capacitance of the two-electron states with respect to the plunger gate of dot R , assuming a simple relation $\varepsilon_R = -|e|V_R$, i.e., assuming unit lever arm between plunger R and dot R , and neglecting the cross-coupling between V_R and other DQD parameters. Generalization of our considerations to a more realistic lever arm structure is straightforward [60, 61].

For convenience, we work in a symmetrized magnetic reference frame [72, 75, 76]. That is, we align the magnetic \tilde{z} axis with the average magnetic field of the two dots,

$$\mathbf{B}_s = (\mathbf{B}_L + \mathbf{B}_R)/2, \quad (2)$$

and define the magnetic \tilde{x} axis such that the difference

$$\mathbf{B}_a = (\mathbf{B}_L - \mathbf{B}_R)/2 \quad (3)$$

of the local magnetic fields lies in the $\tilde{x} > 0$ half-plane of the \tilde{x} - \tilde{z} plane. This implies that the symmetrized and antisymmetrized magnetic field takes the following form in the \tilde{x} - \tilde{y} - \tilde{z} magnetic reference frame:

$$\mathbf{B}_s = (0, 0, B_s), \quad \text{and} \quad \mathbf{B}_a = (B_{a\perp}, 0, B_{a\parallel}), \quad (4)$$

with $B_{a\perp} > 0$. For the rest of the paper, we use example parameter sets where $B_{a\perp}$ and $B_{a\parallel}$ take values of a few milliteslas, whereas $B_s \sim 170$ mT, estimated from data on a micromagnet setup with an in-plane external field of $B_{\text{ext}} = 70$ mT [77].

Throughout the paper, we focus on the vicinity of the (1,1)-(0,2) charge transition and the range of moderate tunneling energies, that is, $|\varepsilon|, |t_0| \ll U$. Hence, we disregard the (2,0) singlet state, and will use the 5×5 matrix representation of the Hamiltonian of Eq. (1). In the

singlet-triplet basis of the (0,2) singlet $|\mathcal{S}\rangle$, and the (1,1) states $|\mathcal{S}_0\rangle, |\mathcal{T}_0\rangle, |\mathcal{T}_+\rangle, |\mathcal{T}_-\rangle$, this matrix representation reads:

$$H = \begin{pmatrix} -\varepsilon & \sqrt{2}t_0 & 0 & 0 & 0 \\ \sqrt{2}t_0 & 0 & g\mu_B B_{a\parallel} & -\frac{g\mu_B B_{a\perp}}{\sqrt{2}} & \frac{g\mu_B B_{a\perp}}{\sqrt{2}} \\ 0 & g\mu_B B_{a\parallel} & 0 & 0 & 0 \\ 0 & -\frac{g\mu_B B_{a\perp}}{\sqrt{2}} & 0 & g\mu_B B_s & 0 \\ 0 & \frac{g\mu_B B_{a\perp}}{\sqrt{2}} & 0 & 0 & -g\mu_B B_s \end{pmatrix}. \quad (5)$$

III. FOUR-STATE DISCRIMINATION WITH QUANTUM CAPACITANCE MEASUREMENT

In a spin-based quantum computer, spin readout can be carried out in various ways. Here, we focus on a situation when two spin qubits are located in two neighboring, but separated, quantum dots, the state of this two-qubit system is unknown to us, and we wish to read them out in the computational basis. This four-state discrimination task can be done via a quantum capacitance measurement, as we describe in this section.

A. Capacitance contrast as a proxy for the quality of four-state discrimination

Before starting the readout process, we assume that the tunnel coupling between the dots is switched off, $t_0 = 0$, and the detuning parameter is tuned to the center of the (1,1) charge configuration, that is, $\varepsilon_L = \varepsilon_R = 0$ and hence $\varepsilon = -U$. We call this the idle position. Readout is done in a different parameter point: detuning is tuned to the vicinity of the (1,1)-(0,2) charge transition, $\varepsilon \approx 0$, and the interdot tunnel coupling t_0 is switched on. We call this the readout position. We plot the energy eigenvalues of the Hamiltonian (1a) as a function of detuning ε in a range of possible readout positions, in Fig. 1(b), for a specific set of model parameters (see caption).

In this work, we assume that the detuning and the tunnel coupling are tuned in a way that their change leads to a perfect state transfer. That is, each computational basis state of the idle position evolves into the corresponding energy eigenstate in the readout position. This is enabled by the absence of level crossings in the parameter-dependent energy spectrum, which, in turn, is assured by the misaligned local magnetic fields in the two dots. Note, however, that optimizing such a high-fidelity state transfer protocol is in general a challenging problem [78–80].

The simultaneous readout of the two qubits can be realized, if the four lowest-energy eigenstates at the readout position have significantly different quantum capacitances. The quantum capacitance of a state can be measured by gate reflectometry, e.g., by probing the reflectance of a resonant circuit (e.g., a lumped-element

tank circuit, or a superconducting resonator) that is connected to a plunger gate of one of the dots [39, 40, 58, 60–63, 65, 81–83].

Fig. 1(c) shows the quantum capacitances of all four relevant states as the functions of the detuning parameter in a range of readout positions, for a specific parameter set (see caption). We label the lowest 4 energy eigenstates, corresponding to the two-qubit computational basis, with $j \in \{1, 2, 3, 4\}$, in ascending order of their energies, that is, $E_1 < E_2 < E_3 < E_4$. The quantum capacitance C_j of energy eigenstate $|\psi_j\rangle$, sometimes also referred to as the charge susceptibility, describes the ‘floppyness’ of the charge, i.e., the change of charge with respect to a change of the gate voltage. For our case (recall that we assume a trivial lever arm structure), this quantum capacitance is expressed as:

$$C_j = \frac{dQ_{R,j}}{dV_R}, \quad (6)$$

where $Q_{R,j} = |e| \langle \psi_j | n_R | \psi_j \rangle$ is the gate charge on plunger R. Together with $\varepsilon_R = -|e|V_R$ and $\varepsilon = \varepsilon_L - \varepsilon_R - U$, these imply the following simple formula:

$$C_j = e^2 \frac{d \langle \psi_j | n_R | \psi_j \rangle}{d\varepsilon}. \quad (7)$$

Fig. 1(c) demonstrates that the readout position can be chosen such that the quantum capacitances of all four states are different at the readout position. Such a detuning value is indicated by the dashed line in Fig. 1(c) (and also shown in panels b and d).

Instrumental noise adds uncertainty to the measured value of the quantum capacitance. Therefore, for high-fidelity state assignment, it is beneficial to have the four capacitance values as far from each other as possible. This implies that a reasonable proxy for the quality of four-state discrimination is the minimum of capacitance differences, which we call the *capacitance contrast*:

$$\Delta C = \min_{i,j \in \{1,2,3,4\}, i < j} |C_j - C_i|. \quad (8)$$

The dependence of the capacitance contrast on the detuning value for our example parameter set is shown as the gray line in Fig. 1(d). As Fig. 1(d) reveals, the dashed lines in Fig. 1(a,b,c) show the detuning value where four-state discrimination has optimal (maximal) capacitance contrast for this example parameter set.

B. Assignment fidelity of four-state discrimination in the presence of amplifier noise

Upon readout, the quantum capacitance of a state cannot be inferred with absolute precision, hence the four-state discrimination procedure will also be noisy. Uncertainty of the measured quantum capacitance is caused, e.g., by amplifier noise, which is often described as a Gaussian broadening of the reflectance peak,

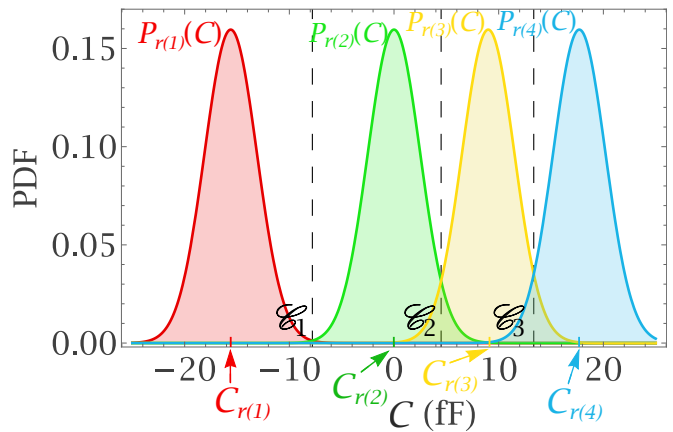


FIG. 2. **Four-state discrimination and readout error in the presence of amplifier noise.** Colored curve $P_{r(j)}$ is the probability density function of the quantum capacitance value inferred from a reflectance measurement performed on state j , in the presence of amplifier noise. Vertical dashed lines are separators used for maximum-likelihood inference, separating the intervals defined in Eq. (11). Means of the probability density functions correspond to the capacitances in Fig. 1(c) along the dashed vertical line: $C_{r(j)} = \{-15.6, 0, 9.0, 17.7\}$ fF. Amplifier noise strength: $\sigma_C = 2.5$ fF. The readout error is determined by the overlaps between the neighboring Gaussians.

whose center is determined by the quantum capacitance [60, 65, 83, 84].

In this subsection, we quantify the effect of this uncertainty on the quality of four-state discrimination. We assume that if the computational basis state j is being measured by reflectometry, then the inferred value of the capacitance is drawn from the Gaussian distribution

$$P_j(C) = \frac{1}{\sqrt{2\pi}\sigma_C} \exp\left(-\frac{(C - C_j)^2}{2\sigma_C^2}\right). \quad (9)$$

Note that the broadening, or *amplifier noise strength*, σ_C is assumed to be the same for all four states. These Gaussian distributions are shown in Fig. 2, for noise strength $\sigma_C = 2.5$ fF, for parameters corresponding to the dashed vertical line in Fig. 1(c).

In the presence of the above-mentioned uncertainty of inferring the quantum capacitance from a reflectometry measurement, it is natural to use the maximum likelihood principle to define the inference rule for 4SD. Informally, this rule is that if we infer the quantum capacitance value of C , then our readout procedure outputs the state label j whose likelihood $P_j(C)$ is maximal.

To formalize the maximum likelihood principle, we introduce the following simple ranking function r . It is a permutation of the state labels, $r : \{1, 2, 3, 4\} \rightarrow \{1, 2, 3, 4\}$, which ranks the capacitances in ascending order: $C_{r(1)} < C_{r(2)} < C_{r(3)} < C_{r(4)}$. For example, the ranking function corresponding to the parameter set of the dashed line in Fig. 1(c) is $r(1) = 2$, $r(2) = 3$, $r(3) = 4$, $r(4) = 1$, implying that indeed, it holds

that $C_{r(1)} < C_{r(2)} < C_{r(3)} < C_{r(4)}$, since it holds that $C_2 < C_3 < C_4 < C_1$.

With this notation, the inference rule can be reformulated as follows:

$$\mathcal{I} : C \mapsto r(j), \text{ if } C \in J_{r(j)}, \quad (10)$$

where

$$J_{r(1)} =]-\infty, \mathcal{C}_1], \quad (11a)$$

$$J_{r(2)} =]\mathcal{C}_1, \mathcal{C}_2], \quad (11b)$$

$$J_{r(3)} =]\mathcal{C}_2, \mathcal{C}_3], \quad (11c)$$

$$J_{r(4)} =]\mathcal{C}_3, \infty[, \quad (11d)$$

and $\mathcal{C}_i = (C_{r(i)} + C_{r(i+1)})/2$. The threshold values \mathcal{C}_1 , \mathcal{C}_2 , and \mathcal{C}_3 , separating the four intervals, are shown as the vertical dashed lines in Fig. 2.

The probability of correct inference of the state j is therefore:

$$\mathcal{F}_j = \int_{J_{r(j)}} dC P_j(C). \quad (12)$$

To quantify the quality of 4SD, we will use the *assignment fidelity*, or *fidelity* for short, which we define as the probability of correct inference, averaged over the four states:

$$\mathcal{F} = \frac{1}{4} \sum_{j=1}^4 \mathcal{F}_j. \quad (13)$$

Alternatively, the quality of 4SD can also be expressed by $1 - \mathcal{F}$, which we call the *assignment infidelity*, or simply *readout error*. Combining Eqs. (9), (10), (11), and (12) with the definition of Eq. (13), the assignment fidelity can also be expressed as:

$$\begin{aligned} \mathcal{F} = & \frac{1}{4} [\Phi(\mathcal{C}_1 - C_{r(1)}) \\ & + (\Phi(\mathcal{C}_2 - C_{r(2)}) - \Phi(\mathcal{C}_1 - C_{r(2)})) \\ & + (\Phi(\mathcal{C}_3 - C_{r(3)}) - \Phi(\mathcal{C}_2 - C_{r(3)})) \\ & + (1 - \Phi(\mathcal{C}_3 - C_{r(4)}))], \end{aligned} \quad (14)$$

where Φ is the cumulative distribution function of a Gaussian with zero mean and standard deviation σ_C :

$$\Phi(C) = \frac{1}{\sqrt{2\pi}\sigma_C} \int_{-\infty}^C dC' \exp\left(-\frac{C'^2}{2\sigma_C^2}\right). \quad (15)$$

The fidelity is bounded by $0.25 \leq \mathcal{F} \leq 1$.

The assignment fidelity as the function of detuning is plotted in Fig. 1(d), as the blue curve, for our example parameter set (see caption), and for amplifier noise strength $\sigma_C = 1$ fF. For these parameters, the fidelity approaches unity for certain detuning values. Furthermore, as expected, the fidelity correlates with the capacitance contrast (gray curve in Fig. 1(d)).

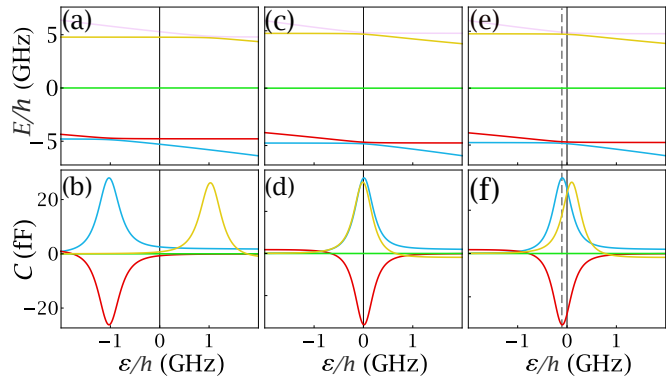


FIG. 3. **Maximizing the capacitance contrast for a fixed magnetic-field configuration.** Energy levels (a,c,e) and quantum capacitances (b,d,f) corresponding to the four lowest-energy states, as functions of detuning ε , for different values of tunneling energy t_0 . Magnetic-field parameters: $(B_{a\parallel}, B_{a\perp}, B_s) = (-2.5, 5, 171.8)$ mT. (a,b) Misaligned lower and upper singlet-triplet anticrossings, at $t_0/h = 3.72$ GHz. (c,d) Aligned anticrossings, at $t_0/h = t_{\text{align}}/h = 3.37$ GHz. (e,f) Slightly misaligned anticrossings, at $t_0/h = 3.41$ GHz, which maximizes the capacitance contrast at the detuning value marked by the dashed vertical line.

C. Maximizing the capacitance contrast

In our model, the capacitance contrast ΔC depends on the gate-tunable parameters ε and t_0 , as well as the magnetic-field parameters B_s , $B_{a\parallel}$, and $B_{a\perp}$. In this subsection, we provide a procedure to maximize the capacitance contrast. To illustrate this procedure, we start from the limiting case where the local magnetic fields in the two dots are similar; that is, $B_{a\parallel}, B_{a\perp} \ll B_s$.

We have seen already in Fig. 1(b) that the misalignment of the local magnetic fields in the two dots, which imply a nonzero value of the parameter $B_{a\perp}$, opens up two singlet-triplet anticrossings in the detuning-dependent energy spectrum. We refer to those as the lower (between E_1 and E_2) and upper (between E_4 and E_5) anticrossings. We argue that the capacitance contrast is maximized when the lower and upper singlet-triplet anticrossings are positioned at slightly different detuning values. To see this, consider the three energy diagrams and three quantum capacitance diagrams shown in Fig. 3.

Fig. 3(a) shows a generic situation, when the singlet-triplet anticrossings are misaligned, that is, their detuning positions are far from each other. In this case, the capacitance contrast is poor for any value of ε : if ε is tuned to, say, the upper (lower) singlet-triplet anticrossing, then $C_2 \approx C_3 \approx 0$ ($C_3 \approx C_4 \approx 0$) and hence $\Delta C \approx 0$.

It is possible to fine-tune the tunneling energy t_0 such that the lower and upper singlet-triplet anticrossings are aligned, that is, are positioned at the same detuning value $\varepsilon = 0$. In the limit of negligibly small magnetic-field

difference $B_a \ll B_s$, this is reached if

$$t_0 = t_{\text{align}} \equiv \frac{1}{\sqrt{2}} g \mu_B B_s. \quad (16)$$

With that choice, shown in Fig. 3(c,d), the two positive-valued capacitance peaks (blue C_1 and yellow C_4) corresponding to the two singlet-triplet bonding states, overlap, yielding, again, a weak capacitance contrast $\Delta C \approx 0$.

However, a maximum of capacitance contrast can be found starting from the latter situation, by a small change δt_{opt} of the tunneling energy t_0 ; that is, setting $t_0 = t_{\text{align}} + \delta t_{\text{opt}}$. E.g., a slight increase of t_0 , as shown in Fig. 3(e,f), displaces the blue (yellow) capacitance peak of C_1 (C_4) to the left (right). Then, for certain values of the detuning ε , all four capacitances become distinguishable; this happens, for example, at the small negative ε value indicated by the dashed vertical line in Fig. 3(e,f).

In what follows, we provide an analytical, perturbative formula for the tunneling energy change δt_{opt} to be applied with respect to Eq. (16), in order to maximize the capacitance contrast. Here, we consider the case $0 < \delta t_{\text{opt}}$. We claim that the capacitance contrast is maximized for tunneling energy $t_0 = t_{\text{align}} + \delta t_{\text{opt}}$ and detuning $\varepsilon = \varepsilon_{\text{opt}}$, with

$$\delta t_{\text{opt}} \approx \frac{\sqrt{2^{2/3} - 1}}{2\sqrt{2}} g \mu_B B_{a\perp} \approx 0.27 g \mu_B B_{a\perp}, \quad (17)$$

and

$$\varepsilon_{\text{opt}} \approx -2\sqrt{2} t_{\text{opt}} \approx -0.77 g \mu_B B_{a\perp}. \quad (18)$$

To provide a perturbative derivation of Eqs. (17) and (18), we split the Hamiltonian H of Eq. (5) to an unperturbed part and a perturbation, the latter being defined as the antisymmetric Zeeman term:

$$H = H_0 + H_1, \quad (19a)$$

$$H_0 = \begin{pmatrix} -\varepsilon & \sqrt{2} t_0 & 0 & 0 & 0 \\ \sqrt{2} t_0 & 0 & 0 & 0 & 0 \\ 0 & 0 & 0 & 0 & 0 \\ 0 & 0 & 0 & g \mu_B B_s & 0 \\ 0 & 0 & 0 & 0 & -g \mu_B B_s \end{pmatrix}, \quad (19b)$$

$$H_1 = g \mu_B \begin{pmatrix} 0 & 0 & 0 & 0 & 0 \\ 0 & 0 & B_{a\parallel} & -\frac{B_{a\perp}}{\sqrt{2}} & \frac{B_{a\perp}}{\sqrt{2}} \\ 0 & B_{a\parallel} & 0 & 0 & 0 \\ 0 & -\frac{B_{a\perp}}{\sqrt{2}} & 0 & 0 & 0 \\ 0 & \frac{B_{a\perp}}{\sqrt{2}} & 0 & 0 & 0 \end{pmatrix}. \quad (19c)$$

From H_0 , we can determine the detuning value corresponding to the lower singlet-triplet anticrossing. We denote the bonding (antibonding) singlet energy eigenstate as $|\mathcal{S}_-(\varepsilon)\rangle$ ($|\mathcal{S}_+(\varepsilon)\rangle$) of H_0 . The corresponding energy eigenvalues of H_0 are

$$E_{\mathcal{S}_{\pm}}(\varepsilon) = -\frac{\varepsilon}{2} \pm \frac{1}{2} \sqrt{\varepsilon^2 + 8t_0^2} \approx -\frac{\varepsilon}{2} \pm \sqrt{2} t_0. \quad (20)$$

Here, the approximation is valid if $\varepsilon \ll t_0$. Furthermore, the polarized triplets have energy eigenvalues

$$E_{\mathcal{T}_{\pm}} = \pm g \mu_B B_s. \quad (21)$$

Eqs. (20) and (21) imply that the detuning values corresponding to the lower and upper singlet-triplet anticrossings, determined by the equations $E_{\mathcal{S}_-}(\varepsilon) = E_{\mathcal{T}_-}$ and $E_{\mathcal{S}_+}(\varepsilon) = E_{\mathcal{T}_+}$, respectively, coincide at $\varepsilon = 0$ if Eq. (16) holds.

The detuning-dependent capacitances $C_1(\varepsilon)$, $C_2(\varepsilon)$ and $C_4(\varepsilon)$ can be expressed analytically from the corresponding 2×2 effective Hamiltonians. We do this at $t_0 = t_{\text{align}}$ and $\varepsilon \approx 0$. Close to the lower singlet-triplet anticrossing, the effective Hamiltonian is obtained by projecting H onto the subspace of $|\mathcal{S}_-(\varepsilon = 0)\rangle$ and $|\mathcal{T}_-\rangle$, yielding:

$$H_{\text{lower}} = \begin{pmatrix} -\varepsilon/2 & g \mu_B B_{a\perp}/2 \\ g \mu_B B_{a\perp}/2 & 0 \end{pmatrix}, \quad (22)$$

where we used the approximation of Eq. (20), and omitted an irrelevant term proportional to the unit matrix.

We express a simple approximative formula for the quantum capacitances C_1 and C_2 from Eq. (22) as follows. We express the bonding and antibonding eigenvectors $\chi_b = (\chi_{b,\mathcal{S}}, \chi_{b,\mathcal{T}})^T$ and $\chi_a = (\chi_{a,\mathcal{S}}, \chi_{a,\mathcal{T}})^T$ of Eq. (22). Then, we approximate the energy eigenstate $|\psi_1\rangle$ as

$$|\psi_1(\varepsilon)\rangle \approx \chi_{b,\mathcal{S}}(\varepsilon) |\mathcal{S}_-(\varepsilon = 0)\rangle + \chi_{b,\mathcal{T}}(\varepsilon) |\mathcal{T}_-\rangle, \quad (23)$$

and $|\psi_2\rangle$ in a similar fashion. Finally, we evaluate the quantum capacitance using Eq. (7), which yields:

$$C_1(\varepsilon) = \frac{e^2}{8} \frac{g^2 \mu_B^2 B_{a\perp}^2}{(\varepsilon^2/4 + g^2 \mu_B^2 B_{a\perp}^2)^{3/2}}. \quad (24)$$

Furthermore, it holds that $C_2(\varepsilon) = -C_1(\varepsilon)$ and $C_4(\varepsilon) = C_1(\varepsilon)$. We will denote the peak value of the capacitance curve $C_1(\varepsilon)$ as $C_{\text{peak}} = e^2/(8g\mu_B B_{a\perp})$.

With a small change δt of the tunneling energy, i.e., setting $t_0 = t_{\text{align}} + \delta t$, the capacitance peaks of C_1 and C_4 are displaced into opposite directions along the detuning axis:

$$C_1(\varepsilon; \delta t) = \frac{e^2}{8} \frac{g^2 \mu_B^2 B_{a\perp}^2}{\left(\left(\frac{\varepsilon}{2} + \sqrt{2} \delta t\right)^2 + g^2 \mu_B^2 B_{a\perp}^2\right)^{3/2}}, \quad (25)$$

and

$$C_4(\varepsilon; \delta t) = \frac{e^2}{8} \frac{g^2 \mu_B^2 B_{a\perp}^2}{\left(\left(\frac{\varepsilon}{2} - \sqrt{2} \delta t\right)^2 + g^2 \mu_B^2 B_{a\perp}^2\right)^{3/2}}. \quad (26)$$

To maximize the capacitance contrast, i.e., to reach $\Delta C = C_{\text{peak}}/2$, parameters ε and δt should be fine-tuned such that $C_1(\varepsilon, \delta t) = C_{\text{peak}}$ and $C_4(\varepsilon, \delta t) = C_{\text{peak}}/2$. These two relations imply the results in Eqs. (17) and (18).

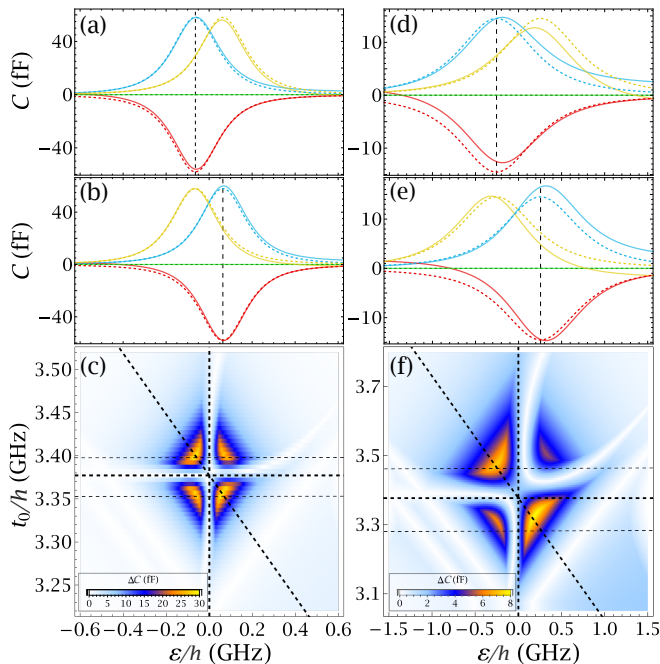


FIG. 4. **Maximizing the capacitance contrast in the detuning-tunneling parameter plane.** (a,b) Detuning dependence of the quantum capacitances of the four states to be discriminated, for magnetic-field parameters $(B_{a\parallel}, B_{a\perp}, B_s) = (-2.5, 3.0, 171.8)$ mT. Tunneling energy: (a) $t_0/h = 3.399$ GHz and (b) $t_0/h = 3.354$ GHz, corresponding to $t_0 = t_{\text{align}} \pm \delta t$, respectively. Solid: exact numerical result. Dashed: perturbative result (e.g., Eq. (25)). (c) Detuning and tunneling dependence of the quantum capacitance contrast ΔC , for the same magnetic-field parameters. Exact, numerical results are shown. Panel (a) [(b)] corresponds to the upper [lower] horizontal cut of panel (c) denoted by the thin dashed line. Horizontal thick dashed line indicates $t_{\text{align}}/h = 3.377$ GHz. Diagonal thick dashed line is the line containing $(\varepsilon, t_0) = (0, t_{\text{align}})$ and the perturbatively determined location of optimal capacitance contrast $(\varepsilon_{\text{opt}}, t_{\text{align}} + \delta t_{\text{opt}})$ (see Eqs. (17),(18)). (d,e,f) Analogous to (a,b,c), with fourfold increased $B_{a\perp}$, i.e., $(B_{a\parallel}, B_{a\perp}, B_s) = (-2.5, 12.0, 171.8)$ mT. Tunneling energy: (d) $t_0/h = 3.47$ GHz, (e) $t_0/h = 3.29$ GHz. Increasing $B_{a\perp}$ from (d) to (f) reduces the number of optimal readout positions (capacitance contrast maxima) from 4 to 2.

As shown in Fig. 4(a,b), the above perturbative results (dashed lines) are in good agreement with numerically exact results (solid lines) in the limit of small B_a (see caption for parameters). In Fig. 4(d,e), where the perturbation $B_{a\perp}$ is increased by a factor of four, the exact results (data points) start to deviate from the perturbative results (solid lines), illustrating the limitations of the above perturbative description.

The capacitance contrast $\Delta C(\varepsilon, t_0)$ as the function of detuning and tunneling energy shows a characteristic quatrefoil pattern in the perturbative regime, as shown in Fig. 4(c). This density plot shows exact numerical results. The quatrefoil pattern signals that in the vicinity

of the anticrossing alignment point $(\varepsilon, t_0) = (0, t_{\text{align}})$, there are four equivalent optimal readout positions maximizing the capacitance contrast.

Moving from Fig. 4(a,b,c) to Fig. 4(d,e,f), we increase $B_{a\perp}$ from 3 mT to 12 mT. In Fig. 4(f), we observe that the fourfold symmetry of the quatrefoil pattern breaks down, leaving only two optimal readout positions instead of four. This characteristic change is in accord with the fact that the peak height of $C_1(\varepsilon)$ is greater than the peak height of $C_4(\varepsilon)$ in the numerical data in Fig. 4(d,e). In turn, this is due to the fact that the quantum capacitance C_1 (C_4) has a contribution from the quantum capacitance of the bonding (antibonding) singlet state $|\mathcal{S}_-\rangle$ ($|\mathcal{S}_+\rangle$), which is positive (negative), and hence increases (decreases) the dominant positive contribution induced by the singlet-triplet anticrossing matrix element.

To summarize, in this subsection we described a procedure to optimize the gate-tunable detuning and tunneling energy parameters to maximize the capacitance contrast. We found that for weak $B_{a\perp}$, there are four equivalent, locally optimal readout points in the (ε, t_0) plane, reducing to two equivalent optima for stronger $B_{a\perp}$. We also provided a perturbative procedure to derive analytical formulas for those optimal readout points.

IV. OPTIMIZING FOUR-STATE DISCRIMINATION IN THE PRESENCE OF RELAXATION

For state-of-the-art readout of solid-state qubits, data acquisition time for a single shot ranges from a few tens of nanoseconds to a few milliseconds. Within that measurement duration, environment-induced relaxation processes have a strong influence on the quality of the readout [60, 84, 85].

In fact, the relaxation time T_1 is often regarded as the maximal reasonable data acquisition time for single-shot readout, since beyond T_1 , the information in the pre-measurement qubit state is mostly erased. Therefore, we compute relaxation times between the relevant states for 4SD, and quantify how these relaxation processes influence the assignment fidelity of 4SD.

In Sec. III B, amplifier noise was taken into account as a random component of the measured quantum capacitance value. Here, we also take into account how the standard deviation σ_C of that random component depends on the measurement duration. We will use the following simple formula to describe this dependence:

$$\sigma_C = \frac{\sqrt{k_B T_n R}}{\kappa V_0 \sqrt{t_{\text{meas}}}} = \frac{c}{\sqrt{t_{\text{meas}}}}. \quad (27)$$

where the second equality defines the constant c . Parameters in Eq. (27), and their values to be used in the following, are as follows (see Ref. [83] and Eqs. (2) and (5) therein for more details): $\kappa = 0.6 \text{ fF}^{-1}$ is the coefficient converting quantum capacitance to reflectance, $V_0 = 3 \mu\text{V}$ is the voltage amplitude of the probe signal

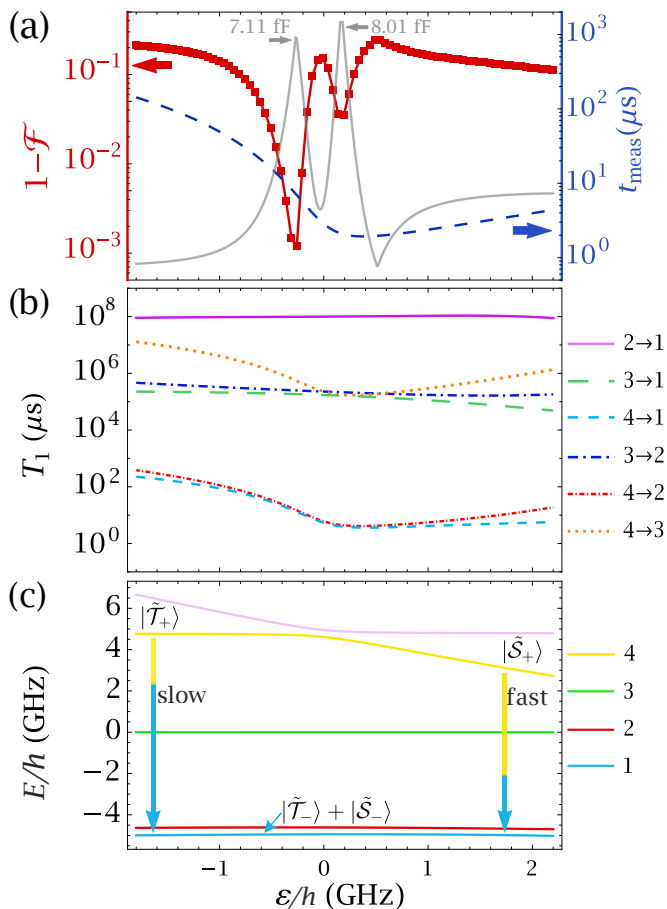


FIG. 5. **Assignment infidelity in the presence of phonon-mediated relaxation and amplifier noise.** (a) Red (left y axis): Average assignment infidelity $1 - \mathcal{F}$ as function of detuning ε , along the diagonal dashed line of Fig. 4(f), at an amplifier noise level $c = 3.136 \text{ fF} \sqrt{\mu\text{s}}$ (see Eq. (27)). Blue dashed (right y axis): measurement time t_{meas} , set as the minimum decay time at 50 mK via Eq. (29). Gray solid line (y axis not shown): capacitance contrast ΔC . Two infidelity dips appear, correlated with the two capacitance-contrast peaks. Difference of the depths of the two infidelity dips is explained by the difference of the relaxation rates. (b) Phonon-mediated downhill relaxation times among the four computational basis states at zero temperature. The $4 \rightarrow 1$ relaxation paths are denoted by arrows; the slow (fast) path requires spin flip (no spin flip). (c) Two-electron DQD energy spectrum. The common x axis of the three panels corresponds to the detuning ε along the diagonal dashed line of Fig. 4(f).

on gate R , $T_n = 4 \text{ K}$ is the effective noise temperature of the amplifier, and $R = 577 \Omega$ is the the resistance of the tank circuit. Together, these yield $c = 3.136 \text{ fF} / \sqrt{\mu\text{s}}$.

Here, we estimate the assignment infidelity for a given set of model parameters. Our procedure is as follows. First, recall that the parameters in our DQD model are ε , t_0 , B_s , $B_{a\parallel}$, B_{\perp} . Additional parameters influencing the relaxation process are the noise strength constant c of Eq. (27), the interdot distance d , and the temperature T . We compute the zero-temperature and finite-

temperature phonon-induced relaxation times $T_{1,j \rightarrow j'}$ among the 4 lowest-energy eigenstates $j, j' \in \{1, 2, 3, 4\}$ of a silicon DQD with interdot distance $d = 100 \text{ nm}$, see details in App. C. We also compute the total decay time of each state via

$$T_j^{-1} = \sum_{j' \neq j} T_{1,j \rightarrow j'}^{-1}. \quad (28)$$

Then we set the measurement time equal to the shortest of the decay times:

$$t_{\text{meas}} = \min_{j \in \{1, 2, 3, 4\}} T_j. \quad (29)$$

Finally, we evaluate the assignment infidelity $1 - \mathcal{F}$ from Eq. (14), such that σ_C is evaluated as $\sigma_C(t_{\text{meas}})$ using Eq. (27), to obtain the assignment fidelity.

Results for the assignment infidelity are shown as the red data points in Fig. 5(a), as the function of detuning ε along the diagonal dashed line of Fig. 4(f). Whereas in Fig. 4(f), the capacitance contrast peaks at positive and negative detuning values are approximately symmetric, in Fig. 5(c), the two infidelity dips are highly asymmetric, with the negative-detuning dip showing much better infidelity.

We explain this asymmetry of the infidelity dips in Fig. 5(a) by the detuning asymmetry of the zero-temperature $4 \rightarrow 1$ relaxation time. The zero-temperature downhill relaxation times calculated from Eq. (C20) are shown in Fig. 5(b). As shown in Fig. 5(b), $T_{1,4 \rightarrow 1}$ is the shortest of the six relaxation times, for all detuning values considered in the figure; hence, at low temperature, this is the relaxation time that controls the measurement time t_{meas} of Eq. (29). As the measurement time is longer for the negative-detuning readout position than for the positive-detuning readout position, the negative-detuning position yields lower assignment infidelity and hence favored.

Finally, we explain the dominance of the relaxation time $T_{1,4 \rightarrow 1}$ and its detuning asymmetry. To facilitate this explanation, we plot the detuning-dependent energy spectrum of the five energy eigenstates in Fig. 5(c). The relaxation processes $4 \rightarrow 1$ and $4 \rightarrow 2$ are at least three orders of magnitude faster than the other processes. These short times scales are explained by the large energy gaps $\sim 2\sqrt{2}t_0$ between the initial and final states, and the large available phonon density of states at the corresponding phonon frequencies. Furthermore, even though in Fig. 5(c) the energy gap $E_4 - E_1$ is slightly asymmetric about $\varepsilon = 0$, this has little effect on the asymmetry of the relaxation times in Fig. 5(b). Instead, that relaxation-time asymmetry is due to spin selection rules (which are quantified by the matrix elements in Fermi's Golden Rule in (C3)). On the one hand, for negative detuning, the initial state 4 is mostly $|\tilde{\mathcal{T}}_+\rangle$, whereas the final state 1 is a balanced hybrid of $|\tilde{\mathcal{T}}_-\rangle$ and the bonding singlet $|\tilde{\mathcal{S}}_-\rangle$; hence relaxation requires spin flip and hence it is slow. On the other hand, for positive detuning, the initial state 4 is mostly the antibonding singlet

$|\mathcal{S}_+\rangle$, whereas the final state is the same as above, hence relaxation does not require spin flip, and hence is fast.

In this section, we focused on the effect of phonon-mediated relaxation processes on the assignment infidelity of 4SD. Relaxation provides a natural upper bound to the measurement time, and hence a lower bound on the assignment infidelity. We have quantified these bounds focusing on a silicon-based double quantum dot with a micromagnet, and identified a single optimal readout position where the spectral and spin structure of the energy eigenstates ensure long relaxation times and hence low assignment infidelity.

V. DISCUSSION

Our results highlight an opportunity to perform 4SD of two-electron states in a DQD with gate reflectometry. In this section, we outline potential ways to refine our analysis further, enabling more precise modeling and more accurate 4SD.

For this work, we assumed that the reflectance measurement in the gate-reflectometry setup including the DQD reveals the quantum capacitances of the spin states. In reality, the relation between the reflectance and the quantum capacitance may have nontrivial ingredients, and modeling those might be important in certain settings.

For example, the reflectance can be influenced by coherent or dissipative dynamical effects in the DQD, such as overdrive effects in terms of Landau-Zener transitions [83], or tunneling capacitance, Sisyphus resistance [61, 62], Hermes admittance [63], etc, which go beyond the adiabatic dynamics that underlies the concept of quantum capacitance. These effects can be made small in the setup we considered, if the resonator's time period is chosen well below the above-microsecond relaxation times (see Fig. 5(b)), and the probe signal is weak enough.

We also note that in this work, for simplicity, we assumed a trivial lever arm structure for the DQD, and hence our estimates for the quantum capacitances are upper bounds, which should be weighted by the lever arm squared [60, 61], to obtain realistic numbers.

A further feature of real devices is charge noise [83], whose main effect can be incorporated into our model as detuning jitter. When too strong, charge noise can lead to an increased readout error via broadening and suppressing the detuning dependence of the capacitance contrast peak (shown as gray in Fig. 1(d)).

The principle of the 4SD procedure we proposed here is material agnostic, as long as either spin-orbit interaction or an inhomogeneous magnetic field provides the spectral anticrossings that are exploited by the method. For n-type silicon DQDs, the case we focused on, a low valley splitting might be a hindrance in general for qubit functionality [4]. For 4SD however, the readout point is in the vicinity of the (1,1)-(0,2) charge transition, hence

the valley excited states are expected to play a much less significant adversarial role than in charge sensing, the latter being performed deep in the (0,2) configuration.

We also anticipate that careful design and characterization of the classical tank circuit of the reflectometry setup is an important requirement to discriminate the four quantum capacitance values. For example, if the tank circuit resonance of the reflectance $\Gamma(C)$ (see, e.g., Fig. (7) of [83]) is narrower than the capacitance contrast ΔC , then discriminating all four states becomes difficult. The recently developed co-simulation tool for hybrid quantum-classical circuits [86] might be especially useful for optimizing the tank circuit design for 4SD.

Another interesting extension of our analysis is to consider advanced inference methods for 4SD. In our work, we assumed that the quantum capacitance is inferred from the time-averaged reflectance signal. Such an approach disregards soft information present in the time trace of the reflectance, and hence can be improved upon by time-trace analysis, for the price of a computational overhead in data processing. One approach is based on hidden Markov models, which has already been studied [87] and implemented [56] in the context of spin qubit readout.

Finally, we note that even if the sensitivity or signal-to-noise ratio of the experiment is not sufficient to perform 4SD in a single shot, a feasible and useful application is to perform multi-shot 4SD. This is a powerful gadget for small-scale quantum experiments, such as quantum state tomography or minimal realizations of quantum algorithms, as demonstrated with superconducting qubits [88–90] and nitrogen-vacancy centers in diamond [91].

VI. CONCLUSIONS

We proposed, modelled, and analyzed an experimental procedure, which enables the discrimination of the four spin states of two electrons in a double quantum dot in a single measurement. The procedure discriminates the quantum capacitances of the four states using gate reflectometry. We described a recipe to maximize the contrast between the quantum capacitances of the four basis states by an appropriate choice of detuning and interdot tunneling parameters. Focusing on silicon double quantum dots equipped with a micromagnet, we quantified how amplifier noise and phonon-mediated relaxation limits the readout infidelity. Our results highlight a realistic opportunity to mitigate the overhead of readout ancilla qubits in a spin-based quantum computer.

ACKNOWLEDGMENTS

We thank B. Kolok, M. Rimbach-Russ and M. Urdampilleta for constructive feedback on the project, and B. Unseld for useful input on the micromagnetic field

configurations. This research was supported by the Ministry of Culture and Innovation (KIM) and the National Research, Development and Innovation Office (NKFIH) within the Quantum Information National Laboratory of Hungary (Grant No. 2022-2.1.1-NL-2022-00004), by the HUN-REN Hungarian Research Network through the HUN-REN-BME-BCE Quantum Technology Research Group, and by the European Union within the Horizon Europe research and innovation programme via the IG-NITE, ONCHIPS, and QLSI2 projects.

Appendix A: Computing quantum capacitance of numerically obtained energy eigenstates without numerical differentiation

In the main text, we expressed the quantum capacitances of the DQD energy eigenstates in Eq. (7). The formula suggests that if the energy eigenstates are computed numerically, then numerical differentiation is required to evaluate the quantum capacitance. This is not the case. In this appendix, we provide a formula to calculate quantum capacitance from first-order time independent perturbation theory, i.e., in a way that does not require the finite-difference numerical evaluation of any derivative. In all of our figures, we used this formula to compute the numerically exact values of quantum capacitances.

We claim that the quantum capacitance formula of Eq. (7) is equivalent to the following formula:

$$C_j = -2e^2 \sum_{k \neq j} \frac{|\langle \psi_k | n_R | \psi_j \rangle|^2}{E_j - E_k}, \quad (\text{A1})$$

or, if the effective lever arm α of the right dot [61] is not 1, then

$$C_j = -2\alpha^2 e^2 \sum_{k \neq j} \frac{|\langle \psi_k | n_R | \psi_j \rangle|^2}{E_j - E_k}. \quad (\text{A2})$$

In our figures, we have used Eq. (A1) to evaluate the quantum capacitance of the energy eigenstates.

One way to derive Eq. (A1) is as follows. Consider the perturbative problem of $\tilde{H} = H + H'$, where $H' = \nu n_R$ is the contribution of a small change of the right plunger gate voltage to the Hamiltonian. Then, Eq. (7) can be expressed as

$$C_j = e^2 \lim_{\nu \rightarrow 0} \frac{\langle \tilde{\psi}_j | n_R | \tilde{\psi}_k \rangle - \langle \psi_j | n_R | \psi_k \rangle}{\nu}, \quad (\text{A3})$$

where the tilde marks the perturbed wave functions. Expressing the perturbed wave functions using first-order perturbation theory, followed by straightforward simplifications, yields Eq. (A1).

Appendix B: A more accurate perturbative description of the quantum capacitances at the singlet-triplet anticrossings

In Sec. III C, we used a perturbative description of the quantum capacitances of the four relevant energy eigenstates in the vicinities of the lower and upper singlet-triplet anticrossings. Here, we argue that this perturbative description can be refined and made more accurate, for the price of slightly more complicated analytical formulas. Here, we describe this refined procedure, and although we omit those more complicated formulas, we do compare the results with the simpler perturbative results and the exact numerical results. In short, this refined method takes into account the quantum capacitances of the bonding and antibonding singlet states, which are neglected by the simplified description of Sec. III C.

We illustrate the procedure for the lower singlet-triplet anticrossing. The derivation refines that in Sec. III C in the step preceding Eq. (22); now we project onto the subspace of $|\mathcal{S}_-(\varepsilon)\rangle$ and $|\mathcal{T}_-\rangle$, i.e., we account for the detuning dependence of the bonding singlet state.

$$H_{\text{lower}} = \begin{pmatrix} E_{\mathcal{S}_-}(\varepsilon) & \frac{g\mu_B B_{a\perp}}{\sqrt{2}} \sin(\theta/2) \\ \frac{g\mu_B B_{a\perp}}{\sqrt{2}} \sin(\theta/2) & -g\mu_B B_s \end{pmatrix}, \quad (\text{B1})$$

where $\tan(\theta) = 2\sqrt{2}t_0/\varepsilon$. We denote the bonding and antibonding eigenvectors of this H_{lower} as $\chi_b(\varepsilon) = (\chi_{b,\mathcal{S}}(\varepsilon), \chi_{b,\mathcal{T}}(\varepsilon))^T$ and $\chi_a = (\chi_{a,\mathcal{S}}(\varepsilon), \chi_{a,\mathcal{T}}(\varepsilon))^T$ of Eq. (B1). Then, the energy eigenstates are expressed as

$$|\psi_1(\varepsilon)\rangle = \chi_{b,\mathcal{S}}(\varepsilon) |\mathcal{S}_-(\varepsilon)\rangle + \chi_{b,\mathcal{T}}(\varepsilon) |\mathcal{T}_-\rangle, \quad (\text{B2a})$$

$$|\psi_2(\varepsilon)\rangle = \chi_{a,\mathcal{S}}(\varepsilon) |\mathcal{S}_-(\varepsilon)\rangle + \chi_{a,\mathcal{T}}(\varepsilon) |\mathcal{T}_-\rangle. \quad (\text{B2b})$$

From these wave function, one can derive analytical results for the quantum capacitances C_1 and C_2 via Eq. (7). Furthermore, C_4 can be described in an analogous way, focusing on the upper singlet-triplet anticrossing.

In Fig. 6, we compare the quantum capacitances derived from the simplified perturbative approach of the main text (Eqs. (25),(26), dotted lines) with the more accurate perturbative method described in this section (Eqs. (B2a),(B2b), dashed lines) and from the numerically exact method (Eq. (A1), solid lines). The dashed and solid lines overlap, illustrating that the refined perturbative approach introduced in this section provides an accurate description of the numerically exact results.

Appendix C: Phonon-induced relaxation rates in a silicon double quantum dot

As discussed in Sec. IV of the main text, phonon-mediated relaxation is an important mechanism limiting the achievable readout fidelity. Here, following earlier studies [75, 76, 92, 93], we describe the details of computing the relaxation times. First, we focus on the case

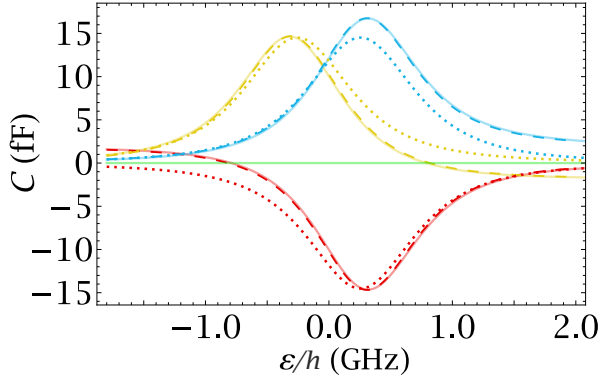


FIG. 6. **Comparison of numerically exact and perturbatively calculated quantum capacitances.** Dotted: quantum capacitances derived from the simplified perturbative approach of the main text (Eqs. (25), (26)). Dashed: result of the more accurate perturbative method described in App. B (Eqs. (B2a),(B2b)). Solid: numerically exact results (Eq. (A1)). Dashed and solid lines overlap, illustrating that the refined perturbative approach provides an accurate description of the numerically exact results. Parameters are the same as in Fig. 4(e).

of zero temperature, and later we generalize to finite temperatures. In our model, we consider the effect of bulk phonons in silicon. The results obtained here are applied in Sec. IV.

In the parameter range we consider, the energy splittings between the electronic states correspond to the frequency range of low-energy acoustic phonons, hence we focus on those. There are three polarization modes, $\lambda \in \{L, T1, T2\}$, where the polarization indices L and T refer to longitudinal and transverse, respectively. The dispersion relations of these low-frequency phonons are linear, $\omega = v_\lambda q$, characterized by their sound velocities v_λ .

Focusing on n-type quantum dots in silicon, we use the Herring-Vogt electron-phonon Hamiltonian [92–96], describing the deformation-potential mechanism:

$$H_{\text{eph}} = \Xi_d \text{Tr}(\epsilon) + \Xi_u \epsilon_{zz}. \quad (\text{C1})$$

Here, Ξ_d is the dilational deformation potential, whereas Ξ_u is the uniaxial deformation potential. Note that for quantum dots, defined in a layer perpendicular to the 001 direction, the electronic wave function is localized in the z and \bar{z} valleys of the silicon band structure. The Hamiltonian of Eq. (C1) contains only the diagonal part of the strain tensor ϵ , which is expressed as:

$$\epsilon_{jj} = i \sqrt{\frac{\hbar}{2\rho V}} \sum_{\mathbf{q}, \lambda} \frac{(\mathbf{e}_{\mathbf{q}, \lambda})_j q_j}{\sqrt{v_\lambda q}} e^{i\mathbf{q} \cdot \mathbf{r}} (a_{\mathbf{q}, \lambda} + a_{-\mathbf{q}, \lambda}^\dagger) \quad (\text{C2})$$

where $j \in (x, y, z)$, and $\mathbf{e}_{\mathbf{q}, \lambda}$ is the polarization vector of the polarization mode λ .

To calculate the zero-temperature relaxation rate between two electronic energy levels, one at higher energy

($|e\rangle$) and the other at lower energy ($|g\rangle$), we use Fermi's Golden Rule:

$$\Gamma_0 = \frac{2\pi}{\hbar} \sum_{\mathbf{q}, \lambda} |\langle g, \mathbf{q}, \lambda | H_{\text{eph}} | e, 0 \rangle|^2 \delta(\Delta E - \hbar v_\lambda q), \quad (\text{C3})$$

where ΔE is the energy difference between the two levels.

1. Relaxation of a charge qubit

First, we consider phonon-assisted relaxation of a charge qubit defined in a double quantum dot. We assume that the relaxation is caused by the interplay of (i) the interdot motion of the electron caused by the phonon-induced on-site energy difference between the two dots (ii) and the different magnetic fields in the two dots.

This mechanism is captured by assuming strongly localized, Dirac-delta-type local basis states on each dot [92]. We take a reference frame such that the center of dot L is at the origin, whereas the center of dot R is at $\mathbf{r}_d = (d, 0, 0)$. Then, the localized basis functions are approximated as $\langle \mathbf{r} | L \rangle = \sqrt{\delta(\mathbf{r})}$ and $\langle \mathbf{r} | R \rangle = \sqrt{\delta(\mathbf{r} - \mathbf{r}_d)}$. The charge-qubit Hamiltonian in the left-right basis defined above reads:

$$H_c = \frac{\varepsilon}{2} \sigma_z + \frac{\Delta}{2} \sigma_x, \quad (\text{C4})$$

where ε is the detuning between the on-site energies, Δ is the interdot tunneling energy, and σ_x and σ_z are Pauli matrices acting on the left-right basis defined above.

We restrict the electronic degrees of freedom of the electron-phonon interaction Hamiltonian H_{eph} to the two above-defined, localized charge-qubit basis states. That is, we define the projection $P = |L\rangle\langle L| + |R\rangle\langle R|$, and use the projected Hamiltonian

$$H_{\text{eph},c} = P H_{\text{eph}} P. \quad (\text{C5})$$

This restriction implies that $H_{\text{eph},c}$ has the same form as the right hand side of Eq. (C1), but in the expression (C2) for the strain tensor, we replace

$$e^{i\mathbf{q} \cdot \mathbf{r}} \mapsto |L\rangle\langle L| + e^{i\mathbf{q} \cdot \mathbf{r}_d} |R\rangle\langle R|. \quad (\text{C6})$$

Correspondingly, in Fermi's Golden Rule (C3), we replace $H_{\text{eph}} \mapsto H_{\text{eph},c}$, and reinterpret the electronic states $|e\rangle$ and $|g\rangle$ as the two-component eigenvectors of H_c in Eq. (C4).

The right hand side of Fermi's Golden Rule (C3) is a sum of 3 contributions from the polarization modes. Without the loss of generality, the polarization vectors $\mathbf{e}_{\mathbf{q}, \lambda}$ for the three polarizations can be chosen as follows:

$$\mathbf{e}_{\mathbf{q},L} = \frac{\mathbf{q}}{q} = \begin{pmatrix} \sin \theta \cos \phi \\ \sin \theta \sin \phi \\ \cos \theta \end{pmatrix}, \quad (\text{C7a})$$

$$\mathbf{e}_{\mathbf{q},T1} = \begin{pmatrix} \cos \theta \cos \phi \\ \cos \theta \sin \phi \\ -\sin \theta \end{pmatrix}, \quad (\text{C7b})$$

$$\mathbf{e}_{\mathbf{q},T2} = \begin{pmatrix} -\sin \phi \\ \cos \phi \\ 0 \end{pmatrix} \quad (\text{C7c})$$

Here, the momentum vector has been parametrized with spherical coordinates $\mathbf{q} = q(\sin \theta \cos \phi, \sin \theta \sin \phi, \cos \theta)$.

The transverse modes do not contribute to dilational term in Eq. (C1), as the polarization vector $\mathbf{e}_{\mathbf{q},T} \perp \mathbf{q}$, such that $\text{Tr}(\epsilon) = 0$. The polarization vector in Eq. (C7c) does not contribute to the second term in Eq. (C1) either.

First, we calculate the contributions from the longitudinal phonons. The diagonal elements of strain tensor, expressed in the orbital basis restricted to $|L\rangle$ and $|R\rangle$, read as follows:

$$\epsilon_{c,jj}^L = i \sqrt{\frac{\hbar}{2\rho V v_L}} \sum_{\mathbf{q}} \frac{q_j^2}{q^{3/2}} (1 - e^{iq_x d}) \frac{\sigma_z}{2} (a_{\mathbf{q},L} + a_{-\mathbf{q},L}^\dagger), \quad (\text{C8})$$

where we used Eqs. (C2), (C6), and (C7a). Here, we omitted a term proportional to σ_0 , describing an equal on-site energy shift on the two dots, which does not contribute to relaxation.

The contribution in Fermi's Golden Rule from the longitudinal phonon due to the dilational deformation potential contains the following matrix element

$$\begin{aligned} M_{\mathbf{q},d}^L &= \langle g, \mathbf{q}L | H_{\text{eph},c} | e, 0 \rangle \\ &= i \Xi_d \sqrt{\frac{\hbar}{8\rho V v_L}} \sum_{\mathbf{q}'} \sqrt{q'} (1 - e^{iq'_x d}) \\ &\quad \times \langle g, \mathbf{q}L | \sigma_z (a_{\mathbf{q}',L} + a_{-\mathbf{q}',L}^\dagger) | e, 0 \rangle. \end{aligned} \quad (\text{C9})$$

Evaluating the matrix element yields:

$$M_{\mathbf{q},d}^L = i \Xi_d \sqrt{\frac{\hbar}{8\rho V v_L}} \langle g | \sigma_z | e \rangle \sum_{\mathbf{q}'} \delta_{\mathbf{q},-\mathbf{q}'} \sqrt{q'} (1 - e^{iq'_x d}). \quad (\text{C10})$$

Finally, evaluating the sum yields:

$$M_{\mathbf{q},d}^L = i \Xi_d \sqrt{\frac{\hbar}{8\rho V v_L}} \langle g | \sigma_z | e \rangle \sqrt{q} (1 - e^{-iq_x d}) \quad (\text{C11})$$

where $|g\rangle, |e\rangle$ are two-component complex vectors as introduced below Eq. (C6).

The uniaxial deformation potential term has only the z-valley contribution from the strain tensor,

$$\epsilon_{c,zz}^L = i \sqrt{\frac{\hbar}{8\rho V v_L}} \sum_{\mathbf{q}} \frac{q_z^2}{q^{3/2}} (1 - e^{iq_x d}) \sigma_z (a_{\mathbf{q},L} + a_{-\mathbf{q},L}^\dagger) \quad (\text{C12})$$

and the corresponding matrix element in Fermi's Golden Rule reads:

$$M_{\mathbf{q},u}^L = i \Xi_u \sqrt{\frac{\hbar}{8\rho V v_L}} \langle g | \sigma_z | e \rangle \sqrt{q} \cos^2 \theta (1 - e^{-iq_x d}). \quad (\text{C13})$$

As discussed above, only the transverse phonons with polarization vector $\mathbf{e}_{\mathbf{q},T1}$ contribute to relaxation, and they do so only through the uniaxial deformation potential. The strain tensor element for the transverse phonons reads:

$$\epsilon_{c,zz}^T = i \sqrt{\frac{\hbar}{8\rho V v_T}} \frac{q_z \mathbf{e}_{z,T1}}{\sqrt{q}} (1 - e^{iq_x d}) \sigma_z (a_{\mathbf{q},T} + a_{-\mathbf{q},T}^\dagger), \quad (\text{C14})$$

and the corresponding matrix element appearing in Fermi's Golden Rule reads:

$$M_{\mathbf{q},u}^T = -i \Xi_u \sqrt{\frac{\hbar}{8\rho V v_T}} \langle g | \sigma_z | e \rangle \sqrt{q} \sin \theta \cos \theta (1 - e^{-iq_x d}). \quad (\text{C15})$$

The zero-temperature relaxation rate calculated using Fermi's Golden Rule (C3), applying Eqs. (C11), (C13) for the longitudinal phonons, and Eq. (C15) for the transverse phonons. We convert the sum over the phonon wavenumber into an integral in spherical coordinates. The rates associated to the emission of longitudinal and transversal phonons, respectively, are evaluated as follows:

$$\begin{aligned}
\Gamma_{0,L} &= \frac{2\pi}{\hbar} \sum_{\mathbf{q}} |M_{\mathbf{q}}^L|^2 \delta(\Delta E - \hbar v_L q) = \frac{2\pi}{\hbar} \sum_{\mathbf{q}} |M_{\mathbf{q},d}^L + M_{\mathbf{q},u}^L|^2 \delta(\Delta E - \hbar v_L q) \\
&= \frac{2\pi}{\hbar} \frac{\hbar}{8\rho V v_L} |\langle g|\sigma_z|e\rangle|^2 \sum_{\mathbf{q}} |(1 - e^{-iq_x d})|^2 q (\Xi_d^2 + 2\Xi_u \Xi_d \cos^2 \theta + \Xi_u^2 \cos^4 \theta) \delta(\Delta E - \hbar v_L q) \\
&= \frac{\pi}{4\rho V v_L} |\langle g|\sigma_z|e\rangle|^2 \frac{V}{(2\pi)^3} \int_0^\infty dq q^3 \int_0^{2\pi} d\phi \int_0^\pi \sin \theta d\theta 2(1 - \cos(q_x d)) (\Xi_d^2 + 2\Xi_u \Xi_d \cos^2 \theta + \Xi_u^2 \cos^4 \theta) \delta(\Delta E - \hbar v_L q) \\
&= \frac{1}{16\pi^2 \rho v_L} |\langle g|\sigma_z|e\rangle|^2 \frac{(\Delta E)^3}{\hbar^4 v_L^4} \int_0^{2\pi} d\phi \int_0^\pi d\theta \sin \theta \left(1 - \cos\left(\frac{\Delta E}{\hbar v_L} d \sin \theta \cos \phi\right) \right) (\Xi_d^2 + 2\Xi_u \Xi_d \cos^2 \theta + \Xi_u^2 \cos^4 \theta) \\
&= \frac{(\Delta E)^3}{16\pi^2 \hbar^4 v_L^5 \rho} |\langle g|\sigma_z|e\rangle|^2 (\Xi_d^2 I_0 + 2\Xi_d \Xi_u I_2 + \Xi_u^2 I_4), \tag{C16a}
\end{aligned}$$

$$\begin{aligned}
\Gamma_{0,T} &= \frac{2\pi}{\hbar} \sum_{\mathbf{q}} |M_{\mathbf{q}}^T|^2 \delta(\Delta E - \hbar v_T q) \\
&= \frac{2\pi}{\hbar} \frac{\hbar \Xi_u^2}{8\rho V v_T} |\langle g|\sigma_z|e\rangle|^2 \frac{V}{(2\pi)^3} \int_0^\infty dq q^3 \int_0^{2\pi} d\phi \int_0^\pi d\theta \sin^3 \theta \cos^2 \theta (1 - \cos(q d \sin \theta \cos \phi)) \delta(\Delta E - \hbar v_T q) \\
&= \frac{\Xi_u^2}{16\pi^2 \rho v_T} |\langle g|\sigma_z|e\rangle|^2 \frac{(\Delta E)^3}{\hbar^4 v_T^4} \int_0^{2\pi} d\phi \int_0^\pi d\theta \sin^3 \theta \cos^2 \theta \left(1 - \cos\left(\frac{\Delta E}{\hbar v_T} d \sin \theta \cos \phi\right) \right) \\
&= \frac{\Xi_u^2 (\Delta E)^3}{16\pi^2 \hbar^4 v_T^5 \rho} |\langle g|\sigma_z|e\rangle|^2 J, \tag{C16b}
\end{aligned}$$

$$\Gamma_0 = \Gamma_{0,L} + \Gamma_{0,T}. \tag{C16c}$$

Here, we have introduced the following integrals:

$$\begin{aligned}
I_n &= \int_0^{2\pi} d\phi \int_0^\pi d\theta \sin \theta (\cos \theta)^n \times \left(1 - \cos\left(\frac{\Delta E}{\hbar v_L} d \sin \theta \cos \phi\right) \right), \\
J &= \int_0^{2\pi} d\phi \int_0^\pi d\theta \sin^3 \theta \cos^2 \theta \times \left(1 - \cos\left(\frac{\Delta E}{\hbar v_T} d \sin \theta \cos \phi\right) \right). \tag{C17}
\end{aligned}$$

2. Relaxation between two-electron energy eigenstates

To describe the two-electron relaxation times shown in Fig. 5, we perform calculations analogous to those presented in the previous subsection. We denote the zero temperature downhill relaxation rate as $\Gamma_0^{j,k} = T_{1,k \rightarrow j}^{-1}$ for each pair j, k of energy eigenstates with $E_j < E_k$. We project our electron-phonon Hamiltonian to the five basis states, whose spatial structure we assume to be Dirac-delta-like. This implies that we apply the following replacement to the plane wave factor in the strain tensor of Eq. (C2):

$$e^{i\mathbf{q}\cdot\mathbf{r}} \mapsto (e^{iq_x d} - 1) |\mathcal{S}\rangle\langle\mathcal{S}|, \tag{C18}$$

where we omitted an irrelevant term proportional to the unit matrix.

With this replacement, we can recycle our results of Eq. (C16) obtained for the charge qubit, for our current goal of describing two-electron relaxation. In fact, the matrix element in Eq. (C16) should be replaced as

$$\langle g|\sigma_z|e\rangle \mapsto 2 \langle g|\mathcal{S}\rangle\langle\mathcal{S}|e\rangle \equiv 2 \langle \psi_j|\mathcal{S}\rangle\langle\mathcal{S}|\psi_k\rangle =: 2A_{j,k}. \tag{C19}$$

Therefore, the zero-temperature relaxation rate is given by

$$\begin{aligned}
\Gamma_0^{j,k} &= \frac{(\Delta E_{j,k})^3 |A_{j,k}|^2}{4\pi^2 \hbar^4 \rho} \\
&\times \left(\frac{\Xi_d^2 I_0^{j,k} + 2\Xi_d \Xi_u I_2^{j,k} + \Xi_u^2 I_4^{j,k}}{v_L^5} + \frac{\Xi_u^2 J^{j,k}}{v_T^5} \right), \tag{C20}
\end{aligned}$$

where the j, k upper index in the spherical integrals specifies the energy gap $\Delta E_{j,k} = E_k - E_j$ between the two states.

We used the following parameter values [96] to calculate the relaxation rates: $d = 100$ nm, $\Xi_u = 8.77$ eV, $\Xi_d = 5$ eV, $v_L = 9330$ m/s, $v_T = 5420$ m/s and $\rho = 2330$ kg/m³. The matrix elements $A_{j,k}$ and the energy gaps $\Delta E_{j,k}$ are calculated numerically for Fig. 5. To obtain finite-temperature downhill and uphill relaxation times, required to evaluate the decay times and the measurement time according to Eqs. (28) and (29), we used the Bose-Einstein factors

$$n_p^{j,k} = (e^{\Delta E_{j,k}/k_B T} - 1)^{-1} \quad (\text{C21})$$

to obtain

$$T_{1,k \rightarrow j}^{-1} = \Gamma_0^{j,k} (1 + n_p^{j,k}) \quad (\text{C22})$$

for the downhill case, and

$$T_{1,j \rightarrow k}^{-1} = \Gamma_0^{j,k} n_p^{j,k} \quad (\text{C23})$$

for the uphill case.

-
- [1] D. Loss and D. P. DiVincenzo, Quantum computation with quantum dots, *Physical Review A* **57**, 120 (1998).
- [2] R. Hanson, L. P. Kouwenhoven, J. R. Petta, S. Tarucha, and L. M. K. Vandersypen, Spins in few-electron quantum dots, *Rev. Mod. Phys.* **79**, 1217 (2007).
- [3] P. Stano and D. Loss, Review of performance metrics of spin qubits in gated semiconducting nanostructures, *Nature Reviews Physics* **4**, 672 (2022).
- [4] F. A. Zwanenburg, A. S. Dzurak, A. Morello, M. Y. Simmons, L. C. L. Hollenberg, G. Klimeck, S. Rogge, S. N. Coppersmith, and M. A. Eriksson, Silicon quantum electronics, *Reviews of Modern Physics* **85**, 961 (2013).
- [5] G. Burkard, T. D. Ladd, A. Pan, J. M. Nichol, and J. R. Petta, Semiconductor spin qubits, *Reviews of Modern Physics* **95**, 025003 (2023).
- [6] A. Chatterjee, P. Stevenson, S. D. Franceschi, A. Morello, N. P. de Leon, and F. Kuemmeth, Semiconductor qubits in practice, *Nature Reviews Physics* **3**, 157 (2021).
- [7] J. M. Elzerman, R. Hanson, L. H. W. van Beveren, B. Witkamp, L. M. K. Vandersypen, and L. P. Kouwenhoven, Single-shot read-out of an individual electron spin in a quantum dot, *Nature* **430**, 431 (2004).
- [8] J. R. Petta, A. C. Johnson, J. M. Taylor, E. A. Laird, A. Yacoby, M. D. Lukin, C. M. Marcus, M. P. Hanson, and A. C. Gossard, Coherent manipulation of coupled electron spins in semiconductor quantum dots, *Science* **309**, 2180 (2005).
- [9] F. H. L. Koppens, C. Buizert, K. J. Tielrooij, I. T. Vink, K. C. Nowack, T. Meunier, L. P. Kouwenhoven, and L. M. K. Vandersypen, Driven coherent oscillations of a single electron spin in a quantum dot, *Nature* **442**, 766 (2006).
- [10] J. Yoneda, K. Takeda, T. Otsuka, T. Nakajima, M. R. Delbecq, G. Allison, T. Honda, T. Kodera, S. Oda, Y. Hoshi, N. Usami, K. M. Itoh, and S. Tarucha, A quantum-dot spin qubit with coherence limited by charge noise and fidelity higher than 99.9%, *Nature Nanotechnology* **13**, 102 (2018).
- [11] Y.-H. Wu, L. C. Camenzind, P. Büttler, I. K. Jin, A. Noiri, K. Takeda, T. Nakajima, T. Kobayashi, G. Scappucci, H.-S. Goan, and S. Tarucha, *Simultaneous high-fidelity single-qubit gates in a spin qubit array* (2025), [arXiv:2507.11918 \[quant-ph\]](https://arxiv.org/abs/2507.11918).
- [12] W. Huang, C. H. Yang, K. W. Chan, T. Tanttu, B. Hensen, R. C. C. Leon, M. A. Fogarty, J. C. C. Hwang, F. E. Hudson, K. M. Itoh, A. Morello, A. Laucht, and A. S. Dzurak, Fidelity benchmarks for two-qubit gates in silicon, *Nature* **569**, 532 (2019).
- [13] X. Xue, M. Russ, N. Samkharadze, B. Undseth, A. Sammak, G. Scappucci, and L. M. K. Vandersypen, Quantum logic with spin qubits crossing the surface code threshold, *Nature* **601**, 343 (2022).
- [14] P. Steinacker, N. D. Stuyck, W. H. Lim, T. Tanttu, M. Feng, S. Serrano, A. Nickl, M. Candido, J. D. Cifuentes, E. Vahapoglu, S. K. Bartee, F. E. Hudson, K. W. Chan, S. Kubicek, J. Jussot, Y. Canvel, S. Beyne, Y. Shimura, R. Loo, C. Godfrin, B. Raes, S. Baudot, D. Wan, A. Laucht, C. H. Yang, A. Saraiva, C. C. Escott, K. D. Greve, and A. S. Dzurak, Industry-compatible silicon spin-qubit unit cells exceeding 99% fidelity, *Nature* **646**, 81 (2025).
- [15] S. G. J. Philips, M. T. Mađzik, S. V. Amitonov, S. L. de Snoo, M. Russ, N. Kalhor, C. Volk, W. I. L. Lawrie, D. Brouse, L. Tryputen, B. P. Wuetz, A. Sammak, M. Veldhorst, G. Scappucci, and L. M. K. Vandersypen, Universal control of a six-qubit quantum processor in silicon, *Nature* **609**, 919 (2022).
- [16] I. F. de Fuentes, E. Raymenants, B. Undseth, O. Pietx-Casas, S. Philips, M. Mađzik, S. de Snoo, S. Amitonov, L. Tryputen, A. Schmitz, A. Matsuura, G. Scappucci, and L. Vandersypen, Running a six-qubit quantum circuit on a silicon spin-qubit array, *PRX Quantum* **7**, 010308 (2026).
- [17] N. W. Hendrickx, W. I. L. Lawrie, M. Russ, F. van Riggelen, S. L. de Snoo, R. N. Schouten, A. Sammak, G. Scappucci, and M. Veldhorst, A four-qubit germanium quantum processor, *Nature* **591**, 580 (2021).
- [18] X. Zhang, E. Morozova, M. Rimbach-Russ, D. Jirovec, T.-K. Hsiao, P. C. Fariña, C.-A. Wang, S. D. Oosterhout, A. Sammak, G. Scappucci, M. Veldhorst, and L. M. K. Vandersypen, Universal control of four singlet-triplet qubits, *Nature Nanotechnology* **20**, 209 (2025).
- [19] J. P. Dehollain, U. Mukhopadhyay, V. P. Michal, Y. Wang, B. Wunsch, C. Reichl, W. Wegscheider, M. S. Rudner, E. Demler, and L. M. K. Vandersypen, Nagaoka ferromagnetism observed in a quantum dot plaquette, *Nature* **579**, 528 (2020).
- [20] C. J. van Diepen, T.-K. Hsiao, U. Mukhopadhyay, C. Reichl, W. Wegscheider, and L. M. K. Vandersypen, Quantum simulation of antiferromagnetic heisenberg chain with gate-defined quantum dots, *Phys. Rev. X* **11**, 041025 (2021).
- [21] T.-K. Hsiao, P. Cova Fariña, S. D. Oosterhout, D. Jirovec, X. Zhang, C. J. van Diepen, W. I. L. Lawrie, C.-A. Wang, A. Sammak, G. Scappucci, M. Veldhorst, E. Demler, and L. M. K. Vandersypen, Exciton trans-

- port in a germanium quantum dot ladder, *Phys. Rev. X* **14**, 011048 (2024).
- [22] F. van Riggelen, W. I. L. Lawrie, M. Russ, N. W. Hendrickx, A. Sammak, M. Rispens, B. M. Terhal, G. Scappucci, and M. Veldhorst, Phase flip code with semiconductor spin qubits, *npj Quantum Information* **8**, 124 (2022).
- [23] K. Takeda, A. Noiri, T. Nakajima, T. Kobayashi, and S. Tarucha, Quantum error correction with silicon spin qubits, *Nature* **608**, 682 (2022).
- [24] B. Undseth, N. Meggiato, Y.-H. Wu, S. R. Katiraeefar, L. Tryputen, S. L. de Snoo, D. D. Esposti, G. Scappucci, E. Greplová, and L. M. K. Vandersypen, *Weight-four parity checks with silicon spin qubits* (2026), [arXiv:2601.23267 \[cond-mat.mes-hall\]](https://arxiv.org/abs/2601.23267).
- [25] M. Veldhorst, J. C. C. Hwang, C. H. Yang, A. W. Leenstra, B. de Ronde, J. P. Dehollain, J. T. Muhonen, F. E. Hudson, K. M. Itoh, A. Morello, and A. S. Dzurak, An addressable quantum dot qubit with fault-tolerant control-fidelity, *Nature Nanotechnology* **9**, 981 (2014).
- [26] M. Veldhorst, C. H. Yang, J. C. C. Hwang, W. Huang, J. P. Dehollain, J. T. Muhonen, S. Simmons, A. Laucht, F. E. Hudson, K. M. Itoh, A. Morello, and A. S. Dzurak, A two-qubit logic gate in silicon, *Nature* **526**, 410 (2015).
- [27] J. T. Muhonen, J. P. Dehollain, A. Laucht, F. E. Hudson, R. Kalra, T. Sekiguchi, K. M. Itoh, D. N. Jamieson, J. C. McCallum, A. S. Dzurak, and A. Morello, Storing quantum information for 30 seconds in a nanoelectronic device, *Nature Nanotechnology* **9**, 986 (2014).
- [28] J. P. Dehollain, S. Simmons, J. T. Muhonen, R. Kalra, A. Laucht, F. Hudson, K. M. Itoh, D. N. Jamieson, J. C. McCallum, A. S. Dzurak, and A. Morello, Bell's inequality violation with spins in silicon, *Nature Nanotechnology* **11**, 242 (2016).
- [29] J. Yoneda, W. Huang, M. Feng, C. H. Yang, K. W. Chan, T. Tanttu, W. Gilbert, R. C. C. Leon, F. E. Hudson, K. M. Itoh, A. Morello, S. D. Bartlett, A. Laucht, A. Saraiva, and A. S. Dzurak, Coherent spin qubit transport in silicon, *Nature Communications* **12**, 4114 (2021).
- [30] A. M. Tyryshkin, S. Tojo, J. J. L. Morton, H. Riemann, N. V. Abrosimov, P. Becker, H.-J. Pohl, T. Schenkel, M. L. W. Thewalt, K. M. Itoh, and S. A. Lyon, Electron spin coherence exceeding seconds in high-purity silicon, *Nature Materials* **11**, 143 (2012).
- [31] K. M. Itoh and H. Watanabe, Isotope engineering of silicon and diamond for quantum computing and sensing applications, *MRS Communications* **4**, 143 (2014).
- [32] A. Mills, C. Guinn, M. Feldman, A. Sigillito, M. Gullans, M. Rakher, J. Kerckhoff, C. Jackson, and J. Petta, High-fidelity state preparation, quantum control, and readout of an isotopically enriched silicon spin qubit, *Physical Review Applied* **18**, 064028 (2022).
- [33] A. M. J. Zwerver, T. Krähenmann, T. F. Watson, L. Lampert, H. C. George, R. Pillarisetty, S. A. Bojarski, P. Amin, S. V. Amitonov, J. M. Boter, R. Caudillo, D. Correas-Serrano, J. P. Dehollain, G. Droulers, E. M. Henry, R. Kotlyar, M. Lodari, F. Lüthi, D. J. Michalak, B. K. Mueller, S. Neyens, J. Roberts, N. Samkharadze, G. Zheng, O. K. Zietz, G. Scappucci, M. Veldhorst, L. M. K. Vandersypen, and J. S. Clarke, Qubits made by advanced semiconductor manufacturing, *Nature Electronics* **5**, 184 (2022).
- [34] S. Neyens, O. K. Zietz, T. F. Watson, F. Luthi, A. Nethewala, H. C. George, E. Henry, M. Islam, A. J. Wagner, F. Borjans, E. J. Connors, J. Corrigan, M. J. Curry, D. Keith, R. Kotlyar, L. F. Lampert, M. T. Mađzik, K. Millard, F. A. Mohiyaddin, S. Pellerano, R. Pillarisetty, M. Ramsey, R. Savytskyy, S. Schaal, G. Zheng, J. Ziegler, N. C. Bishop, S. Bojarski, J. Roberts, and J. S. Clarke, Probing single electrons across 300-mm spin qubit wafers, *Nature* **629**, 80 (2024).
- [35] H. C. George, M. T. Mađzik, E. M. Henry, A. J. Wagner, M. M. Islam, F. Borjans, E. J. Connors, J. Corrigan, M. Curry, M. K. Harper, D. Keith, L. Lampert, F. Luthi, F. A. Mohiyaddin, S. Murcia, R. Nair, R. Nahm, A. Nethewala, S. Neyens, B. Patra, R. D. Raharjo, C. Rogan, R. Savytskyy, T. F. Watson, J. Ziegler, O. K. Zietz, S. Pellerano, R. Pillarisetty, N. C. Bishop, S. A. Bojarski, J. Roberts, and J. S. Clarke, 12-spin-qubit arrays fabricated on a 300 mm semiconductor manufacturing line, *Nano Letters* **25**, 793 (2025).
- [36] M. T. Mađzik, F. Luthi, G. G. Guerreschi, F. A. Mohiyaddin, F. Borjans, J. D. Chadwick, M. J. Curry, J. Ziegler, S. Atanasov, P. L. Bavdaz, E. J. Connors, J. Corrigan, H. E. Ercan, R. Flory, H. C. George, B. Harpt, E. Henry, M. M. Islam, N. Khammassi, D. Keith, L. F. Lampert, T. M. Mladenov, R. W. Morris, A. Nethewala, S. Neyens, R. Otten, L. P. O. Ibarra, B. Patra, R. Pillarisetty, S. Premaratne, M. Ramsey, A. Risinger, J. D. Rooney, R. Savytskyy, T. F. Watson, O. K. Zietz, A. Y. Matsuura, S. Pellerano, N. C. Bishop, J. Roberts, and J. S. Clarke, Operating two exchange-only qubits in parallel, *Nature* **647**, 870 (2025).
- [37] D. Kotekar-Patil, A. Corna, R. Maurand, A. Crippa, A. Orlov, S. Barraud, L. Hutin, M. Vinet, X. Jehl, S. D. Franceschi, and M. Sanquer, Pauli spin blockade in CMOS double quantum dot devices, *physica status solidi (b)* **254**, 10.1002/pssb.201600581 (2017).
- [38] R. Maurand, X. Jehl, D. Kotekar-Patil, A. Corna, H. Bohuslavskiy, R. Laviéville, L. Hutin, S. Barraud, M. Vinet, M. Sanquer, and S. D. Franceschi, A CMOS silicon spin qubit, *Nature Communications* **7**, 13575 (2016).
- [39] M. Urdampilleta, D. J. Niegemann, E. Chanrion, B. Jadot, C. Spence, P.-A. Mortemousque, C. Bäuerle, L. Hutin, B. Bertrand, S. Barraud, R. Maurand, M. Sanquer, X. Jehl, S. D. Franceschi, M. Vinet, and T. Meunier, Gate-based high fidelity spin readout in a CMOS device, *Nature Nanotechnology* **14**, 737 (2019).
- [40] A. Crippa, R. Ezzouch, A. Aprá, A. Amisse, R. Laviéville, L. Hutin, B. Bertrand, M. Vinet, M. Urdampilleta, T. Meunier, M. Sanquer, X. Jehl, R. Maurand, and S. D. Franceschi, Gate-reflectometry dispersive readout and coherent control of a spin qubit in silicon, *Nature Communications* **10**, 2776 (2019).
- [41] S. K. Bartee, W. Gilbert, K. Zuo, K. Das, T. Tanttu, C. H. Yang, N. D. Stuyck, S. J. Pauka, R. Y. Su, W. H. Lim, S. Serrano, C. C. Escott, F. E. Hudson, K. M. Itoh, A. Laucht, A. S. Dzurak, and D. J. Reilly, Spin-qubit control with a milli-kelvin CMOS chip, *Nature* **643**, 382 (2025).
- [42] J. M. Boter, J. P. Dehollain, J. P. van Dijk, Y. Xu, T. Hensgens, R. Versluis, H. W. Naus, J. S. Clarke, M. Veldhorst, F. Sebastiano, and L. M. Vandersypen, Spiderweb array: A sparse spin-qubit array, *Physical Review Applied* **18**, 024053 (2022).
- [43] D. Pataki and A. Pályi, Compiling the surface code to crossbar spin qubit architectures, *Physical Review B* **111**, 115307 (2025).

- [44] L. M. K. Vandersypen, H. Bluhm, J. S. Clarke, A. S. Dzurak, R. Ishihara, A. Morello, D. J. Reilly, L. R. Schreiber, and M. Veldhorst, Interfacing spin qubits in quantum dots and donors—hot, dense, and coherent, *npj Quantum Information* **3**, 34 (2017).
- [45] M. Künne, A. Willmes, M. Oberländer, C. Gorjaew, J. D. Teske, H. Bhardwaj, M. Beer, E. Kammerloher, R. Otten, I. Seidler, R. Xue, L. R. Schreiber, and H. Bluhm, The SpinBus architecture for scaling spin qubits with electron shuttling, *Nature Communications* **15**, 4977 (2024).
- [46] S. M. Patomäki, M. F. Gonzalez-Zalba, M. A. Fogarty, Z. Cai, S. C. Benjamin, and J. J. L. Morton, Pipeline quantum processor architecture for silicon spin qubits, *npj Quantum Information* **10**, 31 (2024).
- [47] K. Ono, D. G. Austing, Y. Tokura, and S. Tarucha, Current rectification by pauli exclusion in a weakly coupled double quantum dot system, *Science* **297**, 1313 (2002).
- [48] R. Schleser, E. Ruh, T. Ihn, K. Ensslin, D. C. Driscoll, and A. C. Gossard, Time-resolved detection of individual electrons in a quantum dot, *Applied Physics Letters* **85**, 2005 (2004).
- [49] D. J. Reilly, C. M. Marcus, M. P. Hanson, and A. C. Gossard, Fast single-charge sensing with a rf quantum point contact, *Applied Physics Letters* **91**, 162101 (2007).
- [50] C. Barthel, M. Kjørgaard, J. Medford, M. Stopa, C. M. Marcus, M. P. Hanson, and A. C. Gossard, Fast sensing of double-dot charge arrangement and spin state with a radio-frequency sensor quantum dot, *Physical Review B* **81**, 161308 (2010).
- [51] T. M. Buehler, D. J. Reilly, R. P. Starrett, A. D. Green-tree, A. R. Hamilton, A. S. Dzurak, and R. G. Clark, Single-shot readout with the radio-frequency single-electron transistor in the presence of charge noise, *Applied Physics Letters* **86**, 143117 (2005).
- [52] W. Jang, J. Kim, M.-K. Cho, H. Chung, S. Park, J. Eom, V. Umansky, Y. Chung, and D. Kim, Robust energy-selective tunneling readout of singlet-triplet qubits under large magnetic field gradient, *npj Quantum Information* **6**, 64 (2020).
- [53] M. Nurizzo, B. Jadot, P.-A. Mortemousque, V. Thiney, E. Chanrion, D. Niegemann, M. Dartiaillh, A. Ludwig, A. D. Wieck, C. Bäuerle, M. Urdampilleta, and T. Meunier, Complete readout of two-electron spin states in a double quantum dot, *PRX Quantum* **4**, 010329 (2023).
- [54] J. Y. Huang, R. Y. Su, W. H. Lim, M. Feng, B. van Straaten, B. Severin, W. Gilbert, N. D. Stuyck, T. Tantt, S. Serrano, J. D. Cifuentes, I. Hansen, A. E. Seedhouse, E. Vahapoglu, R. C. C. Leon, N. V. Abrosimov, H.-J. Pohl, M. L. W. Thewalt, F. E. Hudson, C. C. Escott, N. Ares, S. D. Bartlett, A. Morello, A. Saraiva, A. Laucht, A. S. Dzurak, and C. H. Yang, High-fidelity spin qubit operation and algorithmic initialization above 1 K, *Nature* **627**, 772 (2024).
- [55] V. N. Ciriano-Tejel, M. A. Fogarty, S. Schaal, L. Hutin, B. Bertrand, L. Ibberson, M. F. Gonzalez-Zalba, J. Li, Y.-M. Niquet, M. Vinet, and J. J. Morton, Spin readout of a CMOS quantum dot by gate reflectometry and spin-dependent tunneling, *PRX Quantum* **2**, 010353 (2021).
- [56] C. Lainé, G. A. Oakes, V. Ciriano-Tejel, J. F. Chittock-Wood, L. Peri, M. A. Fogarty, S. M. Patomäki, S. Kubicek, D. F. Wise, R. C. C. Leon, M. F. Gonzalez-Zalba, and J. J. L. Morton, High-fidelity dispersive spin sensing in a tuneable unit cell of silicon MOS quantum dots (2025), [arXiv:2505.10435 \[quant-ph\]](https://arxiv.org/abs/2505.10435).
- [57] J. I. Colless, A. C. Mahoney, J. M. Hornibrook, A. C. Doherty, H. Lu, A. C. Gossard, and D. J. Reilly, Dispersive readout of a few-electron double quantum dot with fast rf gate sensors, *Phys. Rev. Lett.* **110**, 046805 (2013).
- [58] A. West, B. Hensen, A. Jouan, T. Tantt, C.-H. Yang, A. Rossi, M. F. Gonzalez-Zalba, F. Hudson, A. Morello, D. J. Reilly, and A. S. Dzurak, Gate-based single-shot readout of spins in silicon, *Nature Nanotechnology* **14**, 437 (2019).
- [59] E. J. Connors, J. Nelson, and J. M. Nichol, Rapid high-fidelity spin-state readout in Si/Si-Ge quantum dots via rf reflectometry, *Phys. Rev. Appl.* **13**, 024019 (2020).
- [60] F. Vigneau, F. Fedele, A. Chatterjee, D. Reilly, F. Kuemmeth, M. F. Gonzalez-Zalba, E. Laird, and N. Ares, Probing quantum devices with radio-frequency reflectometry, *Applied Physics Reviews* **10**, 021305 (2023).
- [61] R. Mizuta, R. M. Otxoa, A. C. Betz, and M. F. Gonzalez-Zalba, Quantum and tunneling capacitance in charge and spin qubits, *Physical Review B* **95**, 045414 (2017).
- [62] M. Esterli, R. M. Otxoa, and M. F. Gonzalez-Zalba, Small-signal equivalent circuit for double quantum dots at low-frequencies, *Applied Physics Letters* **114**, 253505 (2019).
- [63] L. Peri, M. Benito, C. J. B. Ford, and M. F. Gonzalez-Zalba, Unified linear response theory of quantum electronic circuits, *npj Quantum Information* **10**, 114 (2024).
- [64] A. Russell, A. Zotov, R. Zhao, A. S. Dzurak, M. Fernando Gonzalez-Zalba, and A. Rossi, Gate-based spin readout of hole quantum dots with site-dependent g -factors, *Phys. Rev. Appl.* **19**, 044039 (2023).
- [65] G. Zheng, N. Samkharadze, M. L. Noordam, N. Kalhor, D. Brousse, A. Sammak, G. Scappucci, and L. M. K. Vandersypen, Rapid gate-based spin read-out in silicon using an on-chip resonator, *Nature Nanotechnology* **14**, 742 (2019).
- [66] A. Pfund, I. Shorubalko, K. Ensslin, and R. Leturcq, Suppression of spin relaxation in an InAs nanowire double quantum dot, *Phys. Rev. Lett.* **99**, 036801 (2007).
- [67] J. Danon and Y. V. Nazarov, Pauli spin blockade in the presence of strong spin-orbit coupling, *Physical Review B* **80**, 041301 (2009).
- [68] Z. Scherübl, A. Pályi, G. Frank, I. E. Lukács, G. Fülöp, B. Fülöp, J. Nygård, K. Watanabe, T. Taniguchi, G. Zaránd, and S. Csonka, Observation of spin-orbit coupling induced Weyl points in a two-electron double quantum dot, *Communications Physics* **2**, 108 (2019).
- [69] A. Sen, G. Frank, B. Kolok, J. Danon, and A. Pályi, Classification and magic magnetic field directions for spin-orbit-coupled double quantum dots, *Physical Review B* **108**, 245406 (2023).
- [70] T. Lundberg, D. J. Ibberson, J. Li, L. Hutin, J. C. Abadillo-Uriel, M. Filippone, B. Bertrand, A. Nunnenkamp, C.-M. Lee, N. Stelmashenko, J. W. A. Robinson, M. Vinet, L. Ibberson, Y.-M. Niquet, and M. F. Gonzalez-Zalba, Non-symmetric Pauli spin blockade in a silicon double quantum dot, *npj Quantum Information* **10**, 28 (2024).
- [71] F.-E. von Horstig, L. Peri, V. N. Ciriano-Tejel, S. Barraud, J. A. W. Robinson, M. Benito, F. Martins, and M. F. Gonzalez-Zalba, Electrical readout of spins in the absence of spin blockade, *npj Quantum Information* **11**, 155 (2025).
- [72] O. N. Jouravlev and Y. V. Nazarov, Electron transport

- in a double quantum dot governed by a nuclear magnetic field, *Phys. Rev. Lett.* **96**, 176804 (2006).
- [73] M. Pioro-Ladrière, T. Obata, Y. Tokura, Y. S. Shin, T. Kubo, K. Yoshida, T. Taniyama, and S. Tarucha, Electrically driven single-electron spin resonance in a slanting zeeman field, *Nature Physics* **4**, 776 (2008).
- [74] F. K. Unsel, B. Undseth, E. Raymenants, Y. Matsumoto, S. L. de Snoo, S. Karwal, O. Pietx-Casas, A. S. Ivlev, M. Meyer, A. Sammak, M. Veldhorst, G. Scappucci, and L. M. K. Vandersypen, Baseband control of single-electron silicon spin qubits in two dimensions, *Nature Communications* **16**, 5605 (2025).
- [75] J. M. Taylor, J. R. Petta, A. C. Johnson, A. Yacoby, C. M. Marcus, and M. D. Lukin, Relaxation, dephasing, and quantum control of electron spins in double quantum dots, *Phys. Rev. B* **76**, 035315 (2007).
- [76] J. Danon, Spin-flip phonon-mediated charge relaxation in double quantum dots, *Phys. Rev. B* **88**, 075306 (2013).
- [77] F. K. Unsel, B. Undseth, E. Raymenants, Y. Matsumoto, S. Karwal, O. Pietx-Casas, A. S. Ivlev, M. Meyer, A. Sammak, M. Veldhorst, G. Scappucci, and L. M. K. Vandersypen, [Baseband control of single-electron silicon spin qubits in two dimensions](#) (2024).
- [78] F. Fehse, M. David, M. Pioro-Ladrière, and W. A. Coish, Generalized fast quasiadiabatic population transfer for improved qubit readout, shuttling, and noise mitigation, *Phys. Rev. B* **107**, 245303 (2023).
- [79] S. R. Katirae-Far, Y. Matsumoto, B. Undseth, M. D. Smet, V. Gaultieri, C. V. Meinersen, I. F. de Fuentes, K. Capannelli, M. Rimbach-Russ, G. Scappucci, L. M. K. Vandersypen, and E. Greplova, [Unified evolutionary optimization for high-fidelity spin qubit operations](#) (2025), [arXiv:2503.12256 \[quant-ph\]](#).
- [80] C. Ventura-Meinersen, S. Bosco, and M. Rimbach-Russ, Quantum geometric protocols for fast high-fidelity adiabatic state transfer, *EPJ Quantum Technology* **12**, 125 (2025).
- [81] Y.-Y. Liu, L. Orona, S. F. Neyens, E. MacQuarrie, M. Eriksson, and A. Yacoby, Magnetic-gradient-free two-axis control of a valley spin qubit in $\text{Si}_x\text{Ge}_{1-x}$, *Physical Review Applied* **16**, 024029 (2021).
- [82] E. J. Connors, J. Nelson, L. F. Edge, and J. M. Nichol, Charge-noise spectroscopy of Si/SiGe quantum dots via dynamically-decoupled exchange oscillations, *Nature Communications* **13**, 940 (2022).
- [83] V. D. Maman, M. Gonzalez-Zalba, and A. Pályi, Charge noise and overdrive errors in dispersive readout of charge, spin, and Majorana qubits, *Physical Review Applied* **14**, 064024 (2020).
- [84] C. Barthel, D. J. Reilly, C. M. Marcus, M. P. Hanson, and A. C. Gossard, Rapid single-shot measurement of a singlet-triplet qubit, *Phys. Rev. Lett.* **103**, 160503 (2009).
- [85] B. D'Anjou and G. Burkard, Optimal dispersive readout of a spin qubit with a microwave resonator, *Phys. Rev. B* **100**, 245427 (2019).
- [86] L. Peri, A. Gomez-Saiz, C. J. B. Ford, and M. F. Gonzalez-Zalba, Compact quantum dot models for analog microwave co-simulation, *npj Quantum Information* **11**, 194 (2025).
- [87] M. Spethmann, P. Stano, and D. Loss, Spin-qubit readout analysis based on a hidden Markov model, *Phys. Rev. B* **112**, 115304 (2025).
- [88] S. Filipp, P. Maurer, P. J. Leek, M. Baur, R. Bianchetti, J. M. Fink, M. Göppl, L. Steffen, J. M. Gambetta, A. Blais, and A. Wallraff, Two-qubit state tomography using a joint dispersive readout, *Phys. Rev. Lett.* **102**, 200402 (2009).
- [89] L. DiCarlo, J. M. Chow, J. M. Gambetta, L. S. Bishop, B. R. Johnson, D. I. Schuster, J. Majer, A. Blais, L. Frunzio, S. M. Girvin, and R. J. Schoelkopf, Demonstration of two-qubit algorithms with a superconducting quantum processor, *Nature* **460**, 240 (2009).
- [90] J. M. Chow, L. DiCarlo, J. M. Gambetta, A. Nunnkamp, L. S. Bishop, L. Frunzio, M. H. Devoret, S. M. Girvin, and R. J. Schoelkopf, Detecting highly entangled states with a joint qubit readout, *Phys. Rev. A* **81**, 062325 (2010).
- [91] J. He, Y. Tian, Z. Hu, R. Ye, X. Wang, D. Lu, and N. Xu, Direct readout of a nitrogen-vacancy hybrid-spin quantum register in diamond by analysis of photon arrival time, *Phys. Rev. Appl.* **21**, 054041 (2024).
- [92] P. Boross, G. Széchenyi, and A. Pályi, Valley-enhanced fast relaxation of gate-controlled donor qubits in silicon, *Nanotechnology* **27**, 314002 (2016).
- [93] V. Kornich, C. Kloeffel, and D. Loss, Phonon-assisted relaxation and decoherence of singlet-triplet qubits in Si/SiGe quantum dots, *Quantum* **2**, 70 (2018).
- [94] C. Herring and E. Vogt, Transport and deformation-potential theory for many-valley semiconductors with anisotropic scattering, *Phys. Rev.* **101**, 944 (1956).
- [95] C. Tahan and R. Joynt, Relaxation of excited spin, orbital, and valley qubit states in ideal silicon quantum dots, *Phys. Rev. B* **89**, 075302 (2014).
- [96] P. Boross, G. Széchenyi, D. Culcer, and A. Pályi, Control of valley dynamics in silicon quantum dots in the presence of an interface step, *Phys. Rev. B* **94**, 035438 (2016).